공학석사 학위논문

Study on Self-assembled Giant Nanosheets from Tyrosine-containing Helical Peptides

타이로신 기반 나선형 펩타이드의 대면적 자가조립 나노시트 연구

2017년 2월

서울대학교 대학원

재료공학부

최 익 랑

Abstract

Study on Self-assembled Giant Nanosheets from Tyrosine-containing Helical Peptides

Ikrang Choe

Department of Materials Science and Engineering

The Graduate School

Seoul National University

One of the important challenges in the development of protein-mimetic materials is to understand the sequence specific assembly behavior and the dynamic folding change. Conventional strategies to construct two dimensional nanostructures from the peptides have been limited to β-sheet forming sequences in use of basic building blocks because of their natural tendency to form sheet like aggregations. In this study a new sequence of tyrosine containing peptide was identified, which can form dimers by the disulfide bridge, fold into helix and assemble into macroscopic flat sheet at the

air/water interface. We found that stabilization of helix by the dimerization is a key determinant for maintaining macroscopic flatness.

Proton conduction in biological systems has been an important issue for a better understanding of fundamental life mechanism. In representative proton transfer systems in organisms such as a proton translocation in mitochondria and a proton coupled electron transfer (PCET) of photosystem, it was turned out that several amino acids take an active part as proton transporters. Especially, tyrosine has been known to play a critical role in PCET interplaying with a Ca-Mn cluster in the photosystem II. Moreover it can be polymerized into cross-linked polymers, melanin, possessing a semiconductor-like behavior dependent on hydration. Inspired from this, we made proton conductor with tyrosine containing 2D peptide material by hybridization with inorganic species via the tyrosine oxidation reaction. It was expected to combine the conventional role of tyrosine as a building block of self-assembled structures with the mediating ability as proton conductor. In this process, our attempt also shows that functionalization and/or modification of 2D peptide films can be done through a simple secondary treatment. In perspective of bioelectronics and further applications, it would be a good example for designing versatile platforms for bio-functionalized devices with biocompatible materials.

Keywords: Peptide, Self-assembly, 2-Dimensional Materials, Helix, Disulfide bond, Proton conductor

Student number: 2015-20867

Contents

List of tables

List of figures

Chapter 1. Peptide self-assembly

1.1 Introduction

The ability to design and arrange peptides with a controllable structure and chemical diversity would provide a new class of self-assembled materials with sophisticated functions. One benefits of employing peptide assembly to construct these materials is that the desired bulk properties of the materials can be adjusted by the individual building blocks.[1,2] The range of amino acids allows for tuning to specific applications by varying the primary structure, which influences the physical/chemical properties.[3] Various peptides and their analogues have been employed to prepare interesting nanostructures including fibers,[4-7] tubes,[8-11] ribbons,[12,13] vesicle,[14-16] films,[17-21] and three-dimensional networks[22-24]. The discovery of a general strategy for organizing functional peptides into stable nanostructures with desired dimension and shape is an important focus in developing peptide-based self-assembled materials.

The development of 2D soft nanomaterials occupies a fundamentally important field in materials science because they possess great advantages for lightweight, unique optoelectronic properties, and device fabrication. These advantages offer 2D soft nanomaterials a wide range of potential applications in membrane mimetics, sensing, optoelectronics, catalysis, and

biotechnology.[25-27] There are some examples of such materials like graphene,[28] 2D polymer,[20, 29, 30] highly anisotropic colloid,[31] or bilayer membrane[32]. However, it is very difficult to get scalable nanosheets by the peptide self-assembly and transfer the sheets to other substrates. Although polypeptide-based macroscopic membranes[21] and amyloid-protein fibril-based rigid films[33] exhibit large scale 2D structures, the former possesses inhomogeneous structures composed of bundled fibrils, and the latter can be produced only with a micrometer-scale thickness. Therefore, the development of novel peptide sequences is needed to build scalable, homogeneous 2D nanostructures and explore potential applications of peptide platforms.

Previously, we showed that the YYACAYY sequence can assembly into flat sheets at the air/water interface and simultaneously flatten the top of a water droplet (called faceting).[34] According to modeling and measurements, the elastic modulus of the peptide sheets is approximately 8 GPa, which is stiffer than cancellous bones. In a previous study, we suggested that a tyrosine interaction played an important role in assembly and disulfide formation contributed to the stabilization of the secondary structure based on nuclear magnetic resonance (NMR) analysis. In an effort to understand the detailed mechanism and further generalize the assembly strategy in other peptide sequences, we added phenylalanine, which has been widely used as an assembly motif for various nanostructures. In the peptide sequence design, we intended to maximize synergistic effect of the 2D forming motif (tyrosine, Y),

the strong π-π interaction motif (phenylalanine, F), and the dimer formation motif (cysteine, C). Based on the importance of cysteine in the middle of sequences and two tyrosines at the end of each sequence for facet formation, we designed five sequences (Figure 1.1). These five sequences were investigated, and their assembly behaviors and structures were compared.

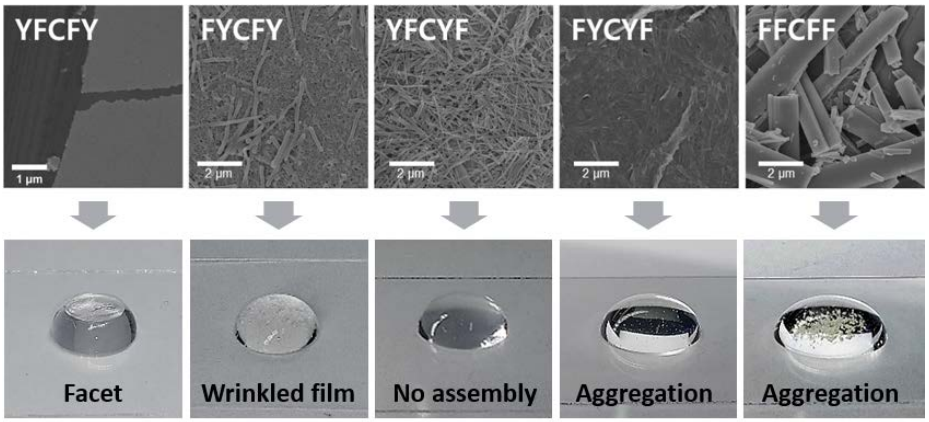

Figure 1.1 SEM images for self-assembled structures of each peptide sequences (upper) and optical images for droplets of 80°C heated peptide solutions (pictures in 10 minutes after drop, lower). Before making solutions all peptide was oxidized for 4 days to make disulfide bond between cysteines.

1.2 Material analysis

1.2.1 Differences of peptide assembly by dimerization

Importantly only the YFCFY (Figure 1.2a) sequence can assemble into giant sheets with faceting (Figure 1.2b) in a similar manner to that of the previous YYACAYY sequence. Immediately after a water droplet containing the peptides was placed on a hydrophobic siliconized glass, a very thin transparent peptide film was formed on the entire surface of the droplet within a few seconds. Then, the top of the droplet was gradually flattened by rigid peptide sheets (Figures 1.2c-e). It is important to note that YFCFY can assemble in pure water but YYACAYY requires buffering conditions (Table 1.1). Additionally, one of the interesting features of YFCFY is that either a fibril-aggregated, rough film or uniformly packed, flat sheet can be formed depending on the initial status of the peptide prior to assembly.

Dimerization between YFCFY monomer was a critical parameter for determining the assembled structures and facet formation. In the sample preparation procedures, the YFCFY monomer was dissolved in deionized water, and the solution was incubated at 80°C. The incubation of the peptides promoted an oxidative reaction, resulting in the formation of YFCFY dimer due to the formation of a disulfide bond between the cysteines. Moreover, the dimer

to monomer ratio could be easily controlled by adjusting the aging time. After 20 hours of incubation, a droplet from the peptide solution produced a clear faceted surface with rigid sheets, which was influenced by the newly formed dimer. However, the YFCFY monomer only produced bumpy films at the interface (Figure 1.3f). To observe the surface of the assembled structure, the samples were prepared using a stamping method (Figure 1.4a). The sample showing rigid sheets at the interface showed 2D homogeneous structure, and the monomer films exhibited a non-uniform, wrinkled morphology (Figure 1.3d). The AFM analysis more clearly showed the differences. The dimer sheets are flat and uniform with a thickness of 10 nm. However, the monomer films are composed of bundled fibrillar fragments (Figures 1.3b, e). To estimate the actual thickness of the dimer sheets on the droplet, the sample was prepared by an extraction method (Figure 1.4b), and its thickness was determined to be nearly 150 nm (Figure 1.3c). Based on these observations, we tried to elucidate the assembly kinetics of YFCFY depending on the dimer ratio and obtain structural information.

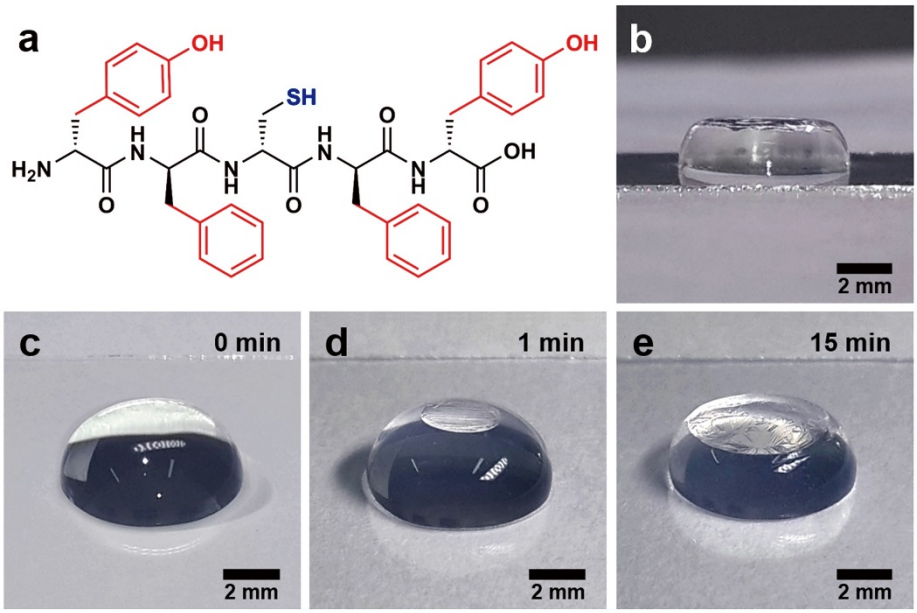

Figure 1.2 Facet formation of water droplets by 2D peptide sheets. (a) Chemical structure of YFCFY. (b) Side view of a faceted water droplet on a siliconized glass. (c-e) Optical images of a water droplet containing YFCFY peptides with the passage of time

Buffer (pH 7)	Concentration			
	50 mM	100 mM	300 mM	500 mM
HEPES	Faceting	Faceting	Faceting	No faceting
Sodium phosphates	Faceting	Faceting	Faceting	No faceting
Sodium citrates	Faceting	Faceting	No faceting	No faceting

Table 1.1 Facet formation of YFCFY dimer depending on buffer conditions. Monomer YFCFY was fully oxidized into dimer form in pure water, then the solution was dried up by lyophilization to get pure dimer peptide. Dimer peptides was dissolved in each buffer solution and concentration was 0.5 mM. As shown in Table, faceting phenomenon does not occur when the buffer concentration is too high. It means that the ions in the buffer partially screen charges of the peptide, resulting inhibition of the self-assembly into large sheets. However, YFCFY can assemble into rigid sheets in several kinds of buffers over a wide range of buffer concentration.

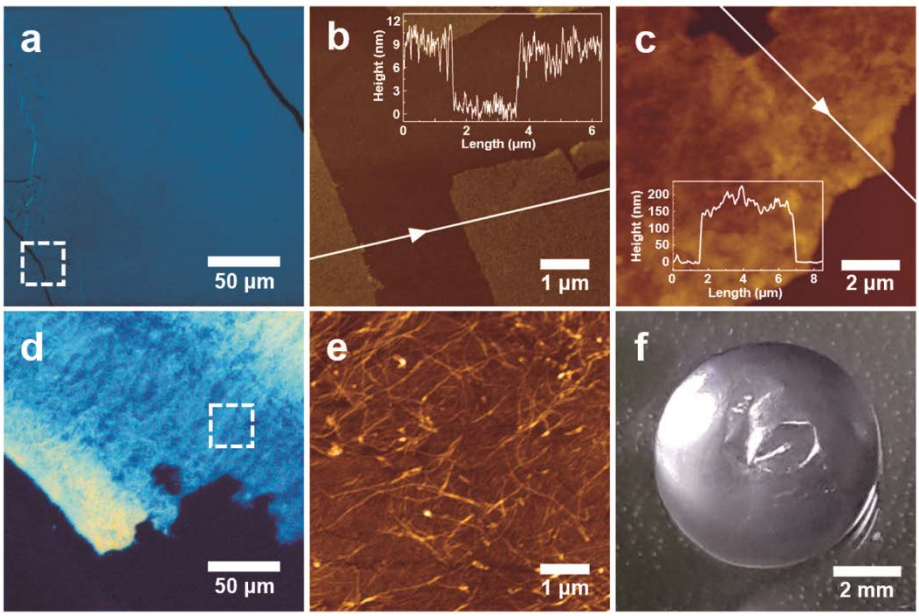

Figure 1.3 Morphology of dimer sheets and monomer films. (a) Optical microscopy image of dimer sheets (b) Atomic force microscopy (AFM) image highlighted with a white box in (a). (c) AFM image of dimer sheets prepared by an extraction method. (d) Optical microscopy image of monomer films transferred by a stamping method. (e) AFM image highlighted with a white box in (d). (f) Top view of the droplet containing monomer films at the air/water interface.

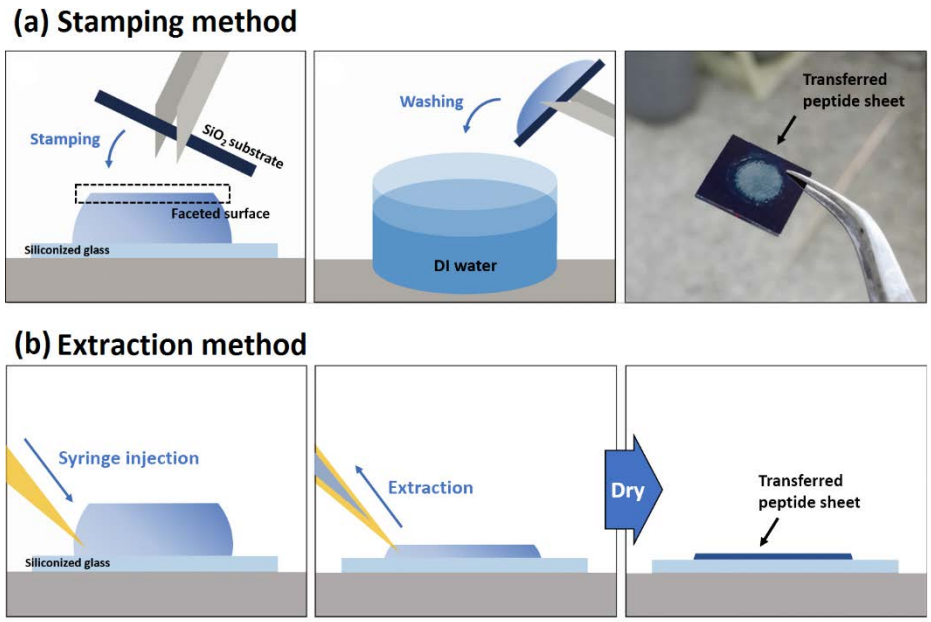

Figure 1.4 (a) Stamping method. Faceted surface was transferred to the silicone oxide substrate by stamping. After that, remaining fibril and fragment were removed by washing the sample with deionized water and dried. (b) Extraction method. A syringe was inserted carefully into faceted droplet. The Inner solution of the droplet was extracted slowly as maintaining sheet on the top and dried.

1.2.2 Kinetic of facet formation

The assembly kinetics and its dependence on the dimer concentration of the initial solutions were investigated using high performance liquid chromatography (HPLC) (Figure 1.5) and electrospray ionization mass spectrometry (ESI-MS) (Figure 1.6). As shown in Figure 1.7, the conversion process from monomer to dimer occurred gradually with a rate of approximately 21% per day and the facet formation was accelerated by increasing the proportion of dimer. The facet formation time of samples containing more than 80% of dimer was less than 5 min, while no faceting was observed for samples containing less than 12% of dimer in solutions. These results suggest that the dimer plays an important role in the formation of rigid peptide sheets and the self-assembly kinetics.

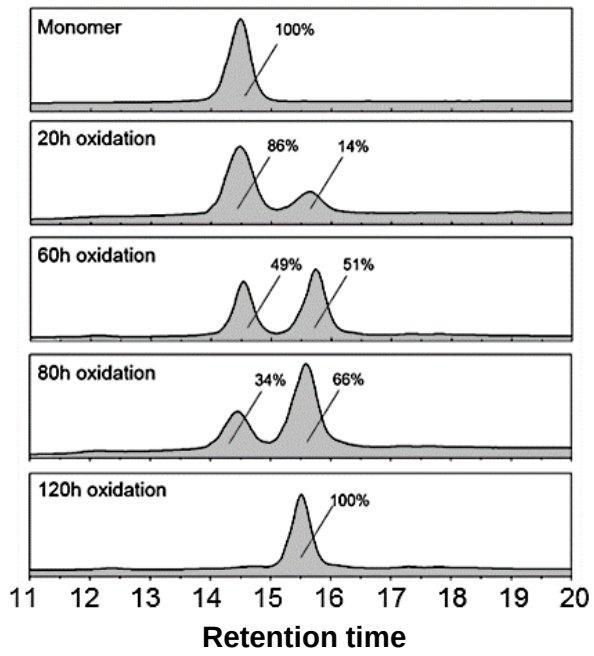

Figure 1.5 High Performance Liquid Chromatography (HPLC) results by the oxidation time for monomer YFCFY

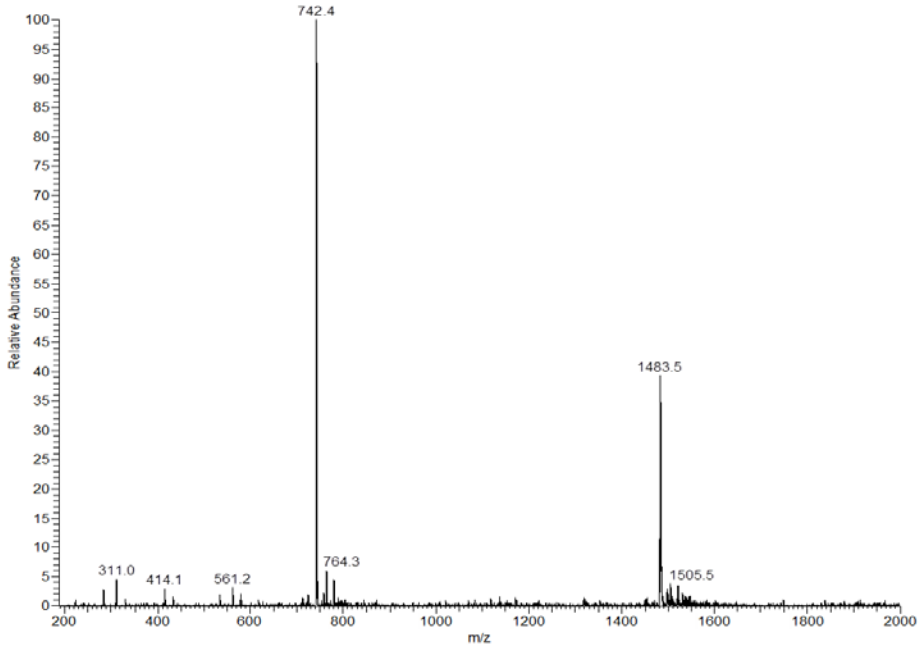

Figure 1.6 Electrospray Ionization Mass Spectrometry (ESI-Mass) data of the second peak (15.5 min) in HPLC. In ESI mass result, the m/z peak at 1483.4 is of dimer YFCFY, the peak at 742.4 is of the monomer YFCFY. Monomer m/z peak was originated from molecules whose disulfide bonding was broken during ionization step in the mass analysis

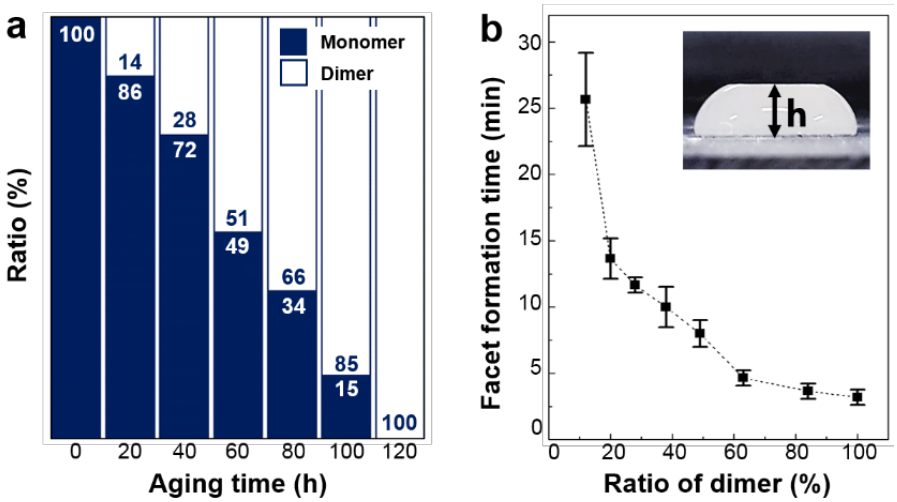

Figure 1.7 Effect of YFCFY dimer on facet formation kinetics. (a) Conversion ratio of monomer to dimer as a function of aging time. (b) Reaction time for facet formation. The time for facet formation of 80 μL droplet was recorded when the distance (=h) between a substrate and the sheet reached 5 mm.

1.2.3 Building block of facet formation

Raman analysis verified that the dimer is indeed a building block for the peptide sheets. The peptide sheet sample was prepared from a solution that was incubated for 2 days and contained more than 50% monomer (see Figure 1.7a). However, as shown in Figure 1.8a, no signal corresponding to the sulfhydryl residues (-SH) at 2570 cm^{-1} was observed in the Raman spectra of the sheets. The sample exhibits a strong signal at 504 cm^{-1} corresponding to a disulfide stretching vibration band, which confirming that dimerization was due to disulfide bond formation between the cysteines.[35,36] In the Raman data of the monomers, a signal corresponding to –SH stretching vibration from the cysteines was observed at 2570 cm^{-1}. These results indicate that only the dimer exists in the peptide sheets.

The Raman spectra also exhibits the additional information about interactions between tyrosine residues. The peak intensity ratio of 850 cm^{-1} to 830 cm^{-1} of monomer is about 0.8, but it increases into 1.05 in assembled peptide sheets. (Figure 1.8b) Those two outstanding peaks called Fermi resonance doublet are commonly discovered in Raman spectra of molecules containing para-substituted benzenes. The peaks at 830 cm^{-1} and 850 cm^{-1} represent the normal mode ν_1 (in-plane breathing fundamental) and the second harmonic $2\nu_{16a}$ (overtone of an out-of-plane ring bending) respectively [37-39]. Their intensity ratio (I_{850}/I_{830}) has been used as a parameter having information

about states of benzene and hydroxyl group in the tyrosine residue. The increased intensity ratio indicates that a substantial portion of the phenolic hydroxyls is strongly hydrogen bonded in the assembled structure[40]. It is known that hydrogen bonding and van der Waals interactions of polar groups including phenols in tightly packed interior of folded protein are more preferred than similar interactions with water in the unfolded state. Those polar groups buried inside of protein contribute to protein stability extensively. Also, hydration state of a hydroxyl group can be changed depending on preferred geometry of a tyrosine[41]. From that it can be suggested that π-π staking among aromatic residues enabled condensed molecular packing at the air/water interface to make hydrophobic interiors, which can induce strongly hydrogen bonded hydroxyl groups.

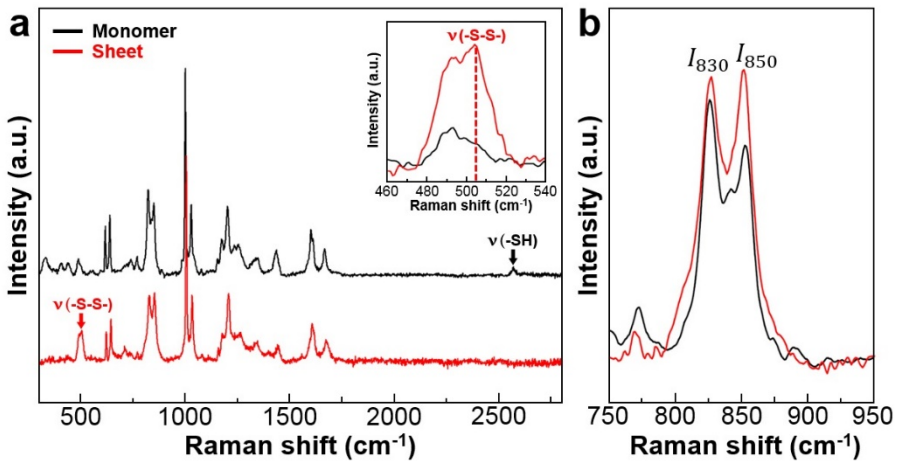

Figure 1.8. Raman analysis of peptide sheets. (a) The Raman spectra of monomers (black line) and peptide sheets (red line). The signal of the range of 460–540cm^{-1} is magnified as an inset. The peak at 2,570 cm^{-1} was from sulfhydryl residue of cysteine (-SH) and 504 cm^{-1} indicated disulfide bonding (-S-S-). (b) The Raman signal from 750 cm^{-1} to 950 cm^{-1} range.

1.3 Conformational analysis

1.3.1 Molecular conformation analysis via circular dichroism spectroscopy

To investigate the molecular conformations of the 2D assembled structures and solvated peptides, solid circular dichroism (CD) and solution-phase CD analysis were performed. As shown in Figure 1.9a, the monomer solution exhibits two positive peaks at 202 nm and 224 nm. The two positive peaks arise due to contributions from chromophores, such as phenols and benzenes, which cause interference with the signal from the amides depending on the local environment.[42-44] The CD measurements of poly-L-tyrosine in a helical conformation revealed that there is the positive Cotton effect from the tyrosine side chain at 225 nm.[45] In addition, strong positive band contribution from tyrosine side chains at approximately 225 nm has been observed in several proteins.[45-48] The positive peak located at approximately 200 nm originated from the amide π-π^* transition and L_a, L_b transition of tyrosine and phenylalanine.[46] Therefore, the positive peaks located at 202 nm and 224 nm in our systems arise from tyrosine, phenylalanine, and the amide transition. The negative peak at 211 nm in the spectra for the dimer solution and the different peak intensity between spectrum of monomer and dimer solutions can be explained by the induced helical components during the dimerization (Figure

1.9a). For the α-helical tyrosine-rich peptide, the strong positive transition observed at approximately 200 nm and 230 nm from the phenols in tyrosines and the two negative bands located at 208 nm and 222 nm from the α-helical backbones are overlapped with each other, leading to a weak negative peak at 217 nm.[45] Likewise, for the dimer solution, the negative peak at 211 nm and the decreased intensity of the positive peaks (202 nm and 224 nm) relative to that of the monomer solution are due to contribution from the π-π^* and n-π^* transitions of the helical conformations.

Conformations of the assembled structures were clearly interpreted using solid CD analysis because the positive Cotton effects of the aromatic side chains were relatively minimized. The CD spectra of the dimer sheets shown in Figure 1.9b contains a strong positive peak at 193 nm and minima at 222 nm (n-π^* transition) and 207 nm (π-π^* transition). These results indicate that the dimer sheets have a typical right-handed helical conformation. The relatively weak intensity of the n-π^* transition compared to that of the π-π^* transition may indicate the presence of a 3_{10}-helix conformation. In detail, the ratio of the CD intensity of the n-π^* transition to that of the π-π^* transition ($[\theta]_{222}/[\theta]_{207}$) for the 3_{10}-helix is in the range of 0.15-0.40,[49-51] and the value for the α-helix is close to 1.[52] Because the value for the dimer sheets is 0.68, the two conformations may exists as equilibrium mixtures. The solid CD spectra of the monomer films contain a strong positive peak at 192 nm and two minima (202 nm and 225 nm), which are substantially shifted from those typical of common helical

conformations. This result implies that the monomer films have a distorted helical conformation. Additionally, a weak positive peak at 240 nm, which appear in the spectra for the dimer sheets, can be assigned to a disulfide bond transition.[53,54] According to a previous study, this peak can be detected in far-UV region when dihedral angle of the disulfide bond deviates from 90°.[55] Therefore, the dihedral angle of the disulfide bond was reorganized during the assembly process.

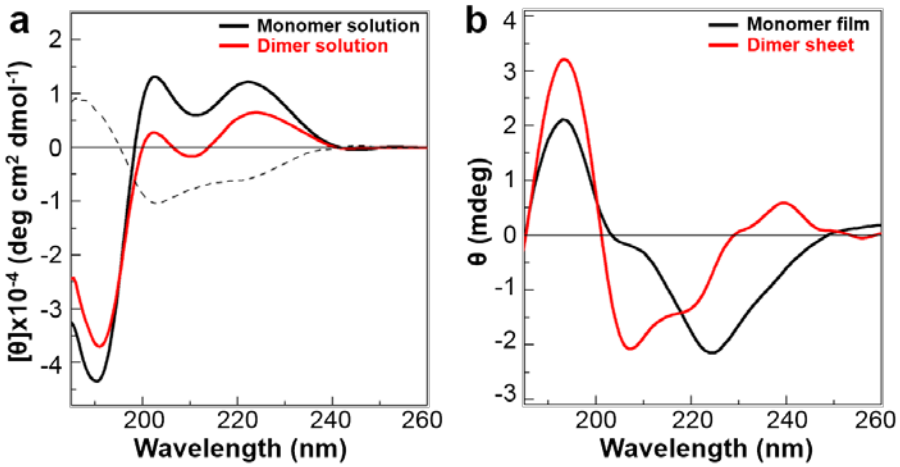

Figure 1.9 Circular dichroism (CD) analysis of YFCFY peptide. (a) The CD spectra of 300 μM YFCFY monomer and 150 μM YFCFY dimer in water. The solid CD spectra are expressed in degree of ellipticity (θ) without concentration terms and the solution CD spectrum are expressed in converted molar ellipticity ([θ]). (b) The CD spectra of monomer film and dimer sheet directly transferred to a quartz cuvette by the stamping method.

1.3.2 Molecular conformation analysis via two-dimensional nuclear magnetic resonance spectroscopy (2D NMR)

The structural differences between the monomer and dimer were confirmed by 2D NMR spectroscopic analysis. The YFCFY peptide gradually changes from the monomers to the dimers due to the formation of disulfide bonds between the cysteine residues. The oxidation reaction was monitored by NMR after 0, 24, 48 hours of reaction. Using 2D total correlation spectroscopy (TOCSY) and 2D nuclear Overhauser effect spectroscopy (NOESY), each amide and alpha proton of YFCFY peptide was assigned.[56,57] The gamma protons of the cysteine were observed at ~2 ppm (Figure 1.10 a,b). As a result of the oxidation reaction, new resonances for Cys3, Phe4, and Tyr5 appeared in both the 2D NOESY and 2D TOCSY spectra (Figure 1.10b and 1.11b), indicating that the YFCFY dimer formed. After 48 hours, complete oxidation of YFCFY was confirmed due to the elimination of the gamma proton peak of Cys3 in the 2D TOCSY spectrum (Figure 1.10c), and only the oxidized form of the peptide exists (Figures 1.10c and 1.11c).

The YFCFY monomer shows sequential NOE connectivities between the neighboring amide and alpha protons and weak NOEs between the neighboring amide and amide protons in the NOESY spectrum (Figure 1.11a, top and bottom), which are observed for a random coil polypeptide. Because YFCFY is rather short and some of the peaks in the 2D NOESY spectra overlap, the

non-sequential NOEs are not clearly shown. For example, the resonance for the amide protons of Cys3 and Tyr5 and the alpha protons of Phe2 and Phe4 are too close in the spectrum (Figure 1.11c, top and bottom). Due to these ambiguous NOE constraints, structure calculation was challenging. Therefore, the helicity of the dimer was confirmed by observing the strong sequential NOEs between neighboring amide protons and additional non-sequential NOEs such as those associated with Phe2-Phe4 and Phe2-Tyr5 (Figure 1.11c). These connectivities represent typical conformations of helix.[58, 59] In accordance with our CD data, this result indicates that the YFCFY dimer forms a helical secondary structure.

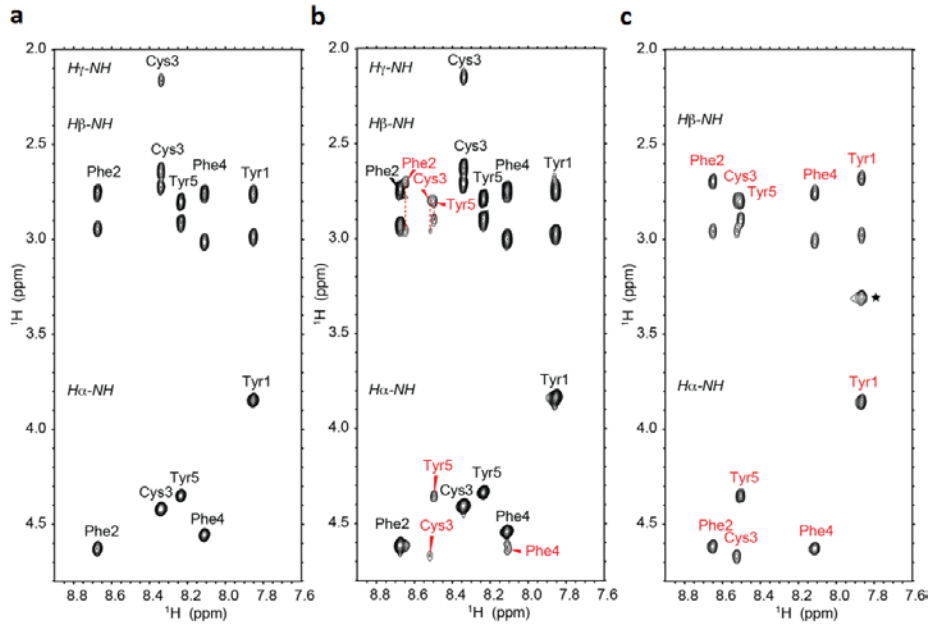

Figure 1.10 2D TOCSY NMR spectra of YFCFY peptide after (a) 0 h, (b) 24h and (c) 48 h of oxidation in DMSO at 60 ºC. Spectra show the correlation between alpha, beta, and gamma protons and amide protons. With increasing reaction time, formation of dimeric YFCFY generates new resonances for Cys3, Phe4, and Tyr5 (b, red). No resonance for Cys3 gamma proton clearly proves the formation of a disulfide bond between Cys residues (c). Star is only shown in the dimeric form of YFCFY that is originated from the TOCSY correlation between the amide proton of Tyr1 and its aromatic proton in the phenol ring.

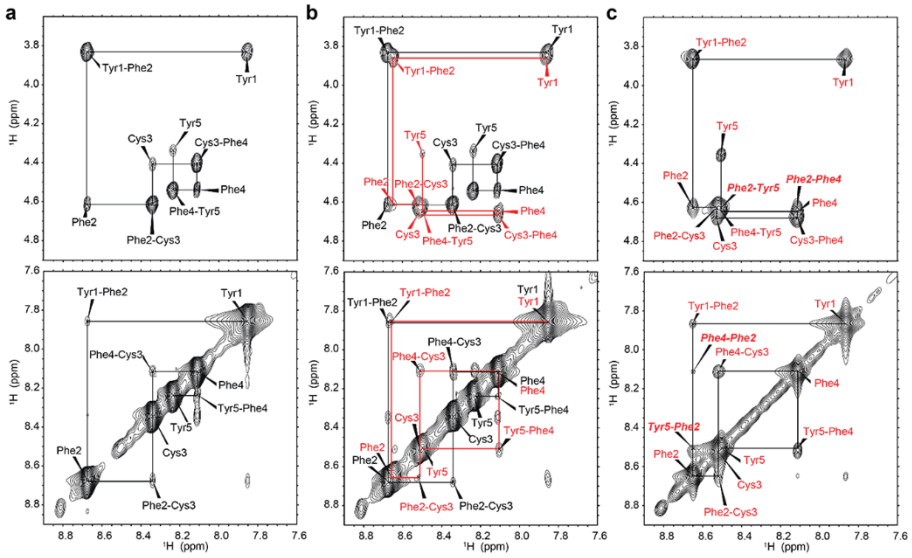

Figure 1.11 2D-NMR analysis of YFCFY peptide. (a-c) NOEs between amide and alpha protons (top) and between amide protons (bottom). Resonances of YFCFY are assigned after (a) 0 h, (b) 24h and (c) 48 h of oxidation in DMSO at 60 ºC. With increasing reaction time, largely shifted resonances for Cys3, Phe4, and Tyr5 appear (b), and non-sequential NOE connectivities (c, bold italic) also appear after completion of oxidation, indicating YFCFY dimer formation. Amino acids from dimer are colored in red.

Chapter 2. Application of 2D Peptide Material

2.1 Introduction

Proton conduction in biological systems has been an important issue for a better understanding of fundamental life mechanism. The most well-known examples are a synthesis of adenosine triphosphate (ATP) driven by proton pumps across the mitochondrial membrane,[73] a light activated proton pumping of bacteriorhodopsin in Archaea,[74] and voltage-regulated proton channels triggering bioluminescence in jellyfish.[75] Along with those long range proton translocations,[76,77] there are several biochemical reactions of relatively short range proton transfers represented by a proton-coupled electron transfer (PCET) occurring in photosystem II[78,79] and ribonucleotide reductases.[80] In the reactions, usually enzymes are in charge of facilitating the transmission of protons using redox active amino acids such as tyrosine and tryptophan in their active site,[81,82] which can mediate an accompanying electron transfer efficiently as charge carriers.[83-85]

A prevalence of proton flows throughout biological processes has been

a great motivation for investigating the bulk proton conductivity of biomolecules, and earlier studies on proton conduction in them enriched our understandings and provided insights about its mechanism and kinetics. Within a context of conventional theories of the proton conduction in bio materials[86], studies has placed value on their abilities of constructing proton channels as a significant factor for the efficient proton transfer, which can form through hydrogen bonded water networks using hydrophilic moieties.[87-89] Recently, Gorodetsky group reported proton conductivity of films made from cephalopod proteins[90] to 0.1 mS/cm and that of films using shark ampullae proteins[91] to 2 mS/cm at room temperature. In a series of the researches, it was noteworthy that amino acids in artificial devices maintained their functions as a proton-donor and mediator building hydrogen bonds with their residue, in suggesting its kinetic can be affected by specific moieties. Recent studies on pigmentary biopolymers in organism, eumelanin, offered another interesting point toward the role of proton conduction in charge transport.[92,93]

Beyond biological systems, there has been numerous attempts to fabricate devices with proton conducting material as one of alternatives

for electronic devices. After alternative energy devices relying on proton conducting materials including fuel cells, electrolysers, and batteries reached the stage of commercialization, a level of proton conductivity became significant parameter determining the performance and efficiency.[94] Owing to the technological needs, researches on proton conduction have encompassed a broad range of materials such as ceramic oxide,[95-100] solid acid,[101-104] metal-organic frameworks[105-109] and polymeric membranes, where the most common is Nafion.[110-114] Hybridization have also received much attention to improve conventional proton conducting polymers with discoveries of introducing hygroscopic inorganic oxides or acids into organic matrix can enhance water absorption, proton conductivity, mechanical and chemical stability. For example, heteropolyacids were extensively adopted as solid conducting fillers due to the large availability of conducting proton within them.[115-117] Hydrophilic particles such as metal oxides, metal phosphate, and zeolites[118] were incorporated to modify water uptake behavior of the original polymer membrane. The consequence properties are usually more than simply the sum of its individual contribution, and rather the strong synergetic effects originated from extensive hybrid interface.

As briefly mentioned, it was turned out that several amino acids take an active part as proton transporters in biological systems. Especially, amino acid having aromatic side chain of hydroxyphenyl group, tyrosine (Tyr, Y) has been known to play a critical role in PCET interplaying with a manganese-calcium cluster in the photosystem II and diiron cluster in ribonucleotide reductase[119,120]. Also, tyrosine can be oxidized and polymerized to eumelanins[121] which show hydration dependent electrical current and high proton conductivity.[92,93] Inspired from the characteristics of tyrosine, we had tried to make proton conductor with tyrosine-rich peptide by oxidant-induced cross-linked system. Herein, we newly synthesized a peptide-based high performance proton conducting films through cross-linking tyrosine by $KMnO_4$ oxidant and hybridization with manganese oxide simultaneously[122]. Previously, we showed that YYACAYY sequence can assembled into giant nano-sheets and suggested the potential for the robust 2-dimensional material with redox active functions.[123] Along with it, herein it was expected to investigate proton conductivity of tyrosine-rich peptide films when hybridized with manganese oxides by using designed peptide sequences of YYACAYY. Our attempt also shows that functionalization of the

peptide films can be done via simple dipping method. The exploration of peptide-based hybrid films as novel proton conductors has not been documented and provides significant implications to both biology and technology. This study indicates that peptide-based hybrid film can suggest a promising new class of proton conductor.

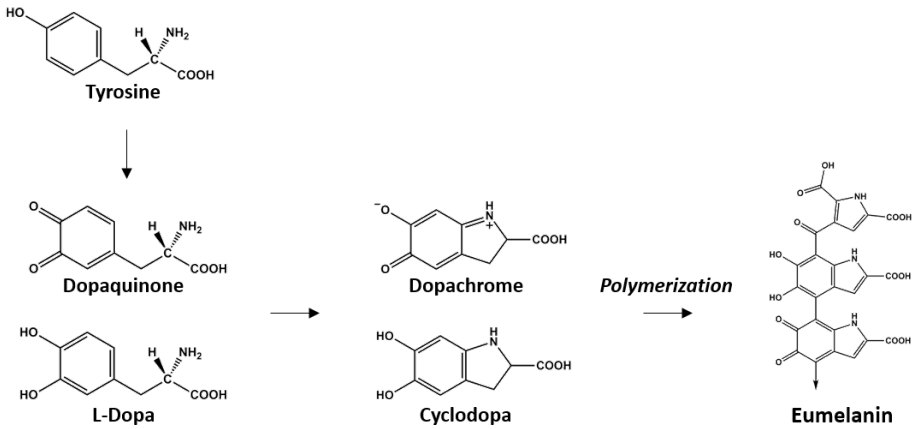

Figure 2.1 A Scheme for the natural polymerizing process of eumelanin

2.2 Material and Analysis

2.2.1 Tyrosine-rich peptide/manganese oxide hybrid material

Tyrosine-containing peptide was hybridized with manganese oxide by using potassium permanganate and their characterizations were carried out. A reaction of tyrosine oxidation was used to involve manganese component into peptide film. A process for fabrication of these peptide-inorganic hybrid film was schematized in figure 1a. A 40 μL drop of YYACAYY peptide solution in HFIP (160 mg mL^{-1}) was placed on a 1 cm × 1 cm cleaned quartz. To allow evaporation of the residual solvent, the peptide film was annealed 150 °C for 30 minutes and rested for another 30 minutes at room temperature. After then the film was immersed into 30 mM solution of potassium permanganate ($KMnO_4$) in deionized water for 15 minutes, in which a deposition of manganese oxide (MnO_x) occurred in the film and peptide/MnOx hybrid composite were made as products. The hybrid film was rinsed with deionized water three times to remove the remaining solution in it and water on surface was eliminated with nitrogen blower. In the reaction the transparent peptide film turned to light brown translucent hybrid film (Figure 2.4a, e) and before-and-after images of two films from optical microscopy (Figure 2.4b, f) showed clear distinction. Noticeable differences were also observed in microstructure

of the films investigated by afm (Figure 2.4c, g) and cross-section TEM (figure 2.4d, h), which showed that interposing of MnO_x into stacked peptides roughened the surface of the film.

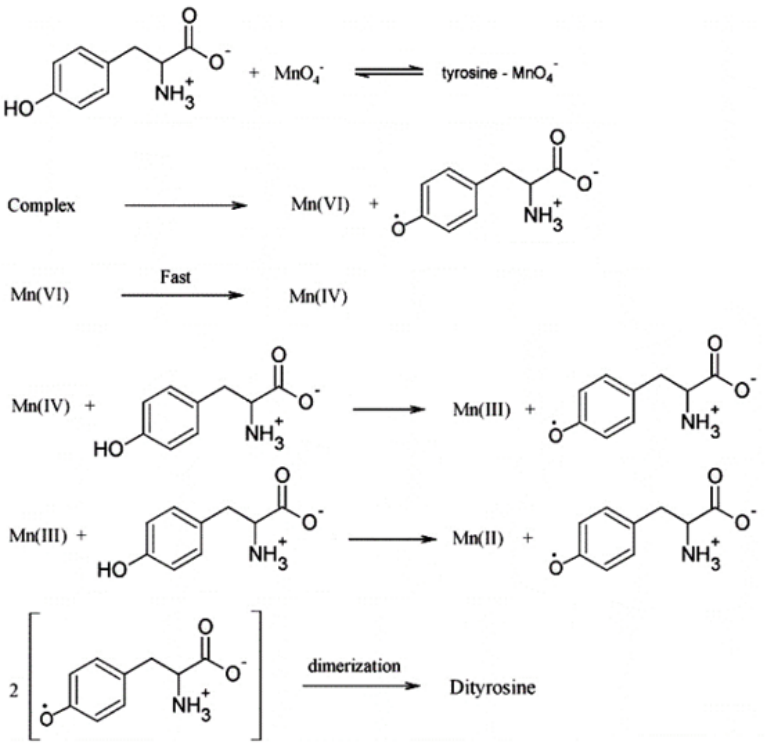

Figure 2.2 Scheme for synthesis of dityrosine using $KMnO_4$

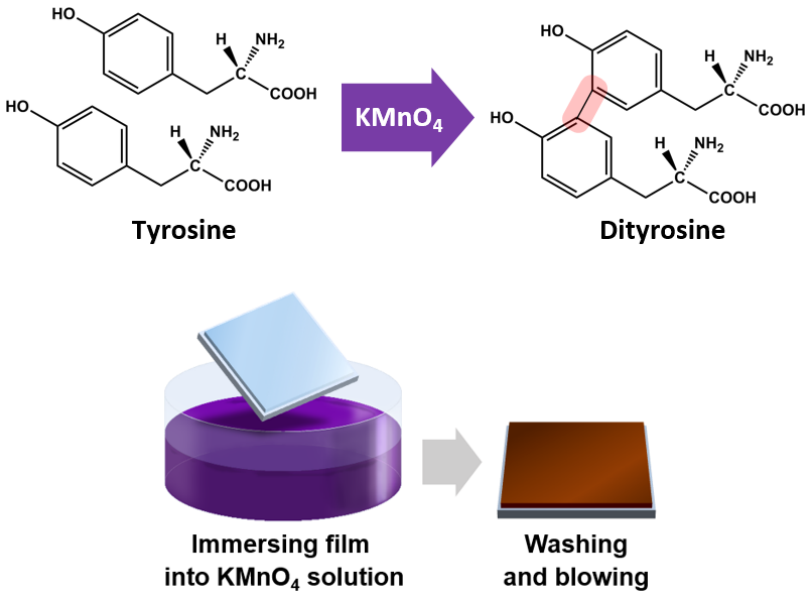

Figure 2.3 Schematic diagram describing the fabrication process of peptide/manganese oxide hybrid film.

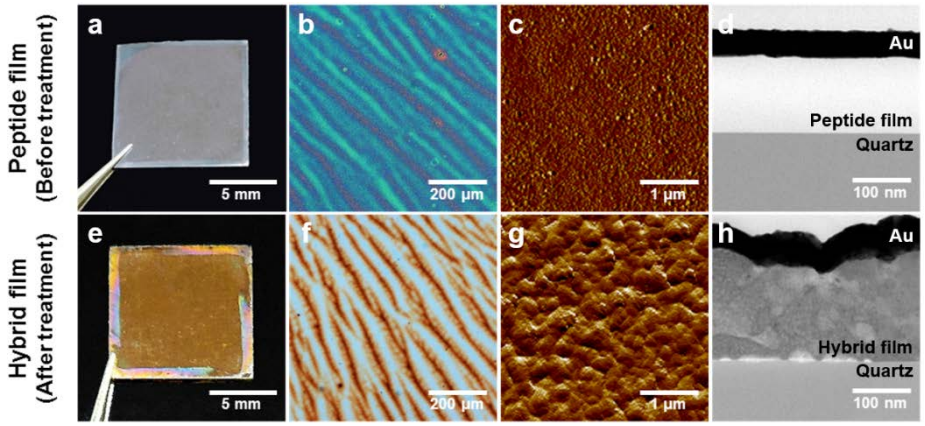

Figure 2.4 A before-and-after comparison of the films with $KMnO_4$ treatment by optical images (a,e), optical microscopy images (b,f), atomic force microscopy (AFM) images (c,g) and transmission electron microscopy (TEM) images (d,h)

2.2.2 Characterizations of manganese oxides

Further detailed investigations were done for each component in peptide/MnOx hybrid film. In this study, the electron microscopy and various spectroscopic tools were employed to analyze the materials including high resolution transmission electron microscopy (HR-TEM), x-ray absorption near-edge structure (XANES), ultraviolet-visible spectroscopy (UV-vis), and photoluminescence spectroscopy (PL).

Manganese components were analyzed with HR-TEM and XANES. In observation of high resolution TEM images (Figure 2.5) it was founded that crystalline MnO_x particles were embedded in peptide film and their diameter were 6 (± 1) nm. The d spacing values of these crystalline parts were 2.41 Å, 2.77 Å which matched MnO_2 and Mn_2O_3, respectively, and the values corresponding to MnO were also observed. These results suggested that the hybrid film composed with various kinds of partially crystalline MnO_x. To understand the chemical nature of MnO_x in hybrid film, we carried out X-ray absorption spectroscopy which provides information about molecular structure and valence state of the materials.[124] Based on Edge shift data from the K-edge XANES spectra of the film and other representative manganese oxides (Figure 2.6), the average valence of manganese in the film was calculated 3.28. Interestingly, with these analysis it was thought other manganese oxides

having various oxidation states were also exist in the hybrid films, although MnO_2 has been known that main product of the oxidative reaction using $KMnO_4$ with organic components.[125-127] Furthermore, we performed Energy-dispersive X-ray spectroscopy (EDX) mapping in TEM images of a thin sample milled by focused ion beam (FIB) (Figure 2.7), the results showed MnO_x were formed throughout the film and they accounted for 30.5 % of the hybrid film which confirmed by inductively coupled plasma - mass spectroscopy (ICP-MS) (Table 2.1).

Peptide before and after $KMnO_4$ treatment were studied with several spectroscopic tools. UV-vis spectroscopy has been used to characterize peptides, especially for which consist amino acid having aromatic ring in their side chain such as phenylalanine, tyrosine, and tryptophan. In figure 2.8, the only peak was observed at 280 nm in peptide film which is a known value of tyrosine and it came from aromatic side chain of tyrosine.[128] In spectrum of the hybrid film it was founded that this peak was remaining after reacting with $KMnO_4$, which indicated that products still had 4-hydroxyphenyl group. Broadening of its bandwidth up to ~320 nm was ascribing to formation of extended π-conjugate system and it has been known that the amount of this red shift depends on the degree of conjugation in the molecule.[129-131] In addition, a new absorbance band of hybrid film spectrum was obtained at around 400 nm region, which was speculated from manganese oxide.[132-135]

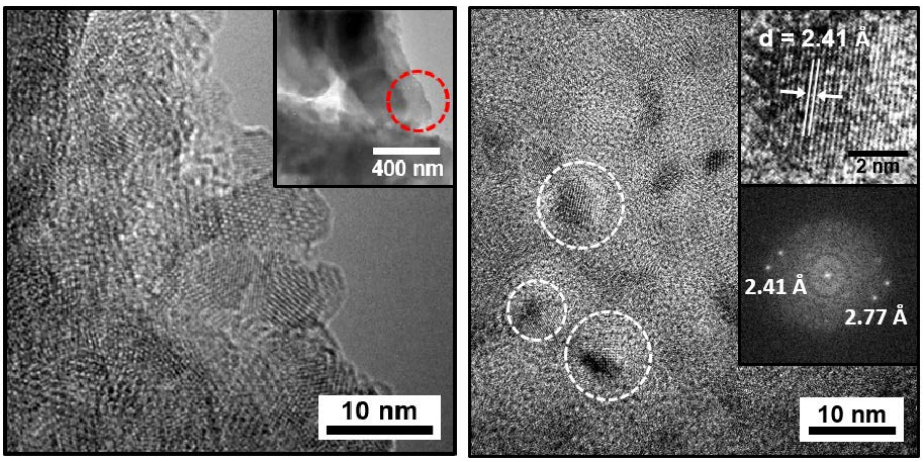

Figure 2.5 Images from high resolution transmission electron microscopy (TEM) for peptide/manganese oxide hybrid films

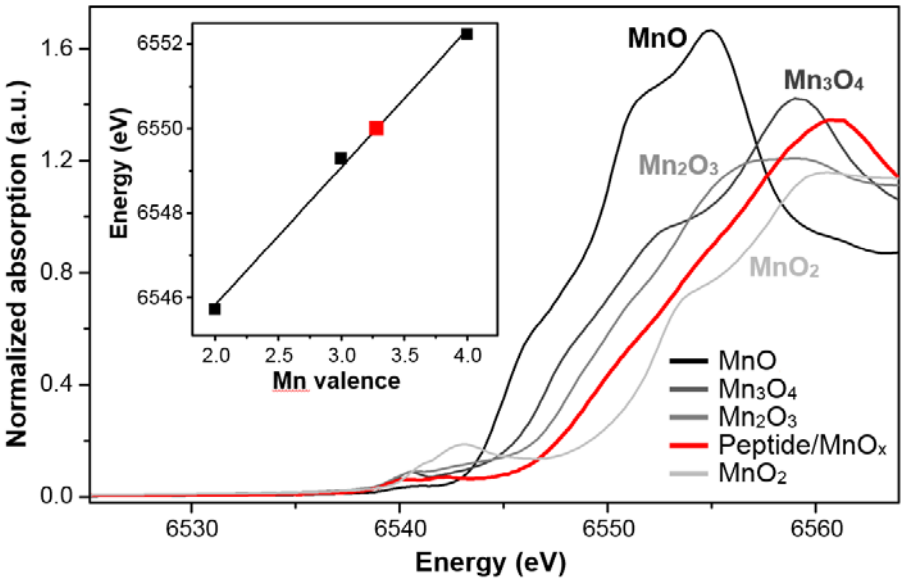

Figure 2.6 X-ray absorption near edge structure (XANES) spectra at the Manganese (Mn) K-edge for various Manganese oxide and the hybrid film. The inset is a fitted linear relationship between energy and oxidation state of Mn.

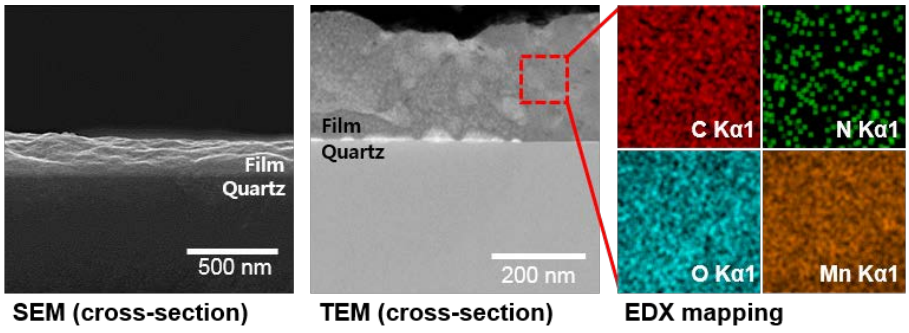

Figure 2.7 Energy-dispersive X-ray spectroscopy (EDX) mapping in TEM images of a thin sample milled by focused ion beam (FIB)

ICP-MS Data Sheet	
Sample	**Mn**
Mn-Peptide	269585704.3
*All samples were analyzed three times and averaged(Mean).	

Table 2.1 The concentration of elements in samples (ppb=μg/kg).

2.2.3 Characterizations of peptide in hybrid films

To investigate more about tyrosine derivatives formed after $KMnO_4$ treatment, photoluminescence (PL) properties were measured. As shown in figure 2.9, in-situ PL emission spectra of 280 nm and 350 nm excitation were collected by titration of $KMnO_4$ solution. In spectra of emission scan from excitation of 280 nm, the band appeared at 305 nm which is the characteristic of tyrosine[135-137] and its intensity deceased by titration of $KMnO_4$ solution. At the same time, upon excitation at 350 nm, the fluorescence spectra of the products displayed three emission maxima at 413 nm, 435 nm, and 465 nm with gradual enhancement of their peak intensity by the reaction. Because the region of 410–415 nm in emission spectrum has been used for detecting the existence of dityrosine fluorometrically,[138,139] so the growth of band at 413 nm revealed that dityrosine was present in product of the reaction. The other two bands would be due to contributions from derivatives of oxidized tyrosine although the exact products and a detailed mechanism of oxidation process for this require further investigation.

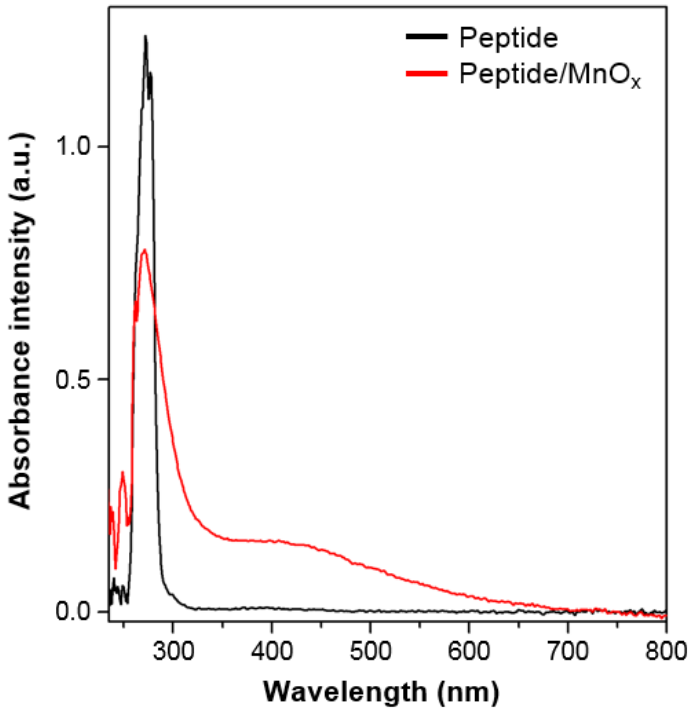

Figure 2.8 UV-VIS spectra of peptide film (black) and hybrid film (red)

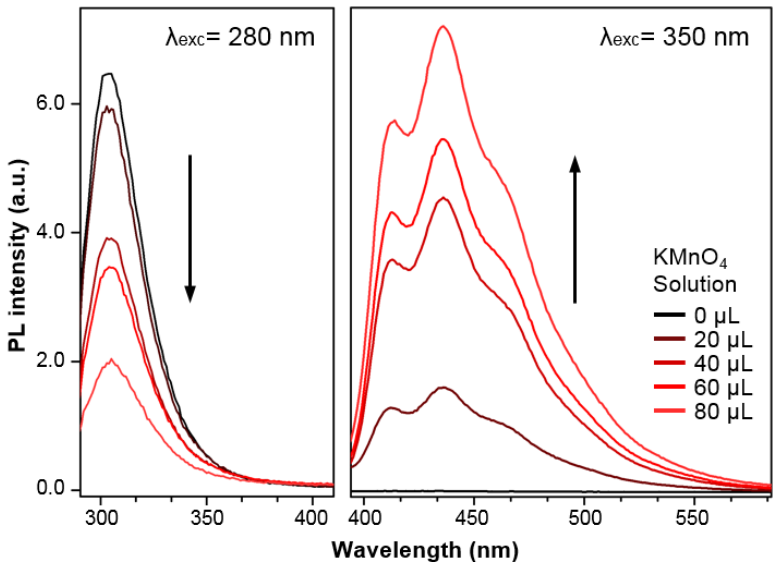

Figure 2.9 Photoluminescence spectrum of 280 nm and 350 nm excitation recorded by titration of $KMnO_4$ solution. The color changed from black (peptide only) to red.

2.3 Measurements and discussion

2.3.1 Electrochemical impedance spectroscopy (EIS)

Bulk protonic conductivity of fabricated hybrid film in two terminal devices were screened by measuring current as a function of voltage and electrochemical impedance spectroscopy (EIS). For measurements of current−voltage (I-V) characteristics of the film, we put the limitation to applied voltage below 1.0 V to eliminate contributions of water electrolysis, of which thermoneutral voltage has been known as 1.5V. During the bias was provided into the device from -1.0 V to +1.0 V, the current were recorded under the condition with a certain degree of relative humidity (RH) from vacuum to 90 %RH and results were plotted in Figure 2.10. In the results, it was founded that the conductivity of the film was affected by RH and the film became more conductive as surroundings of the device got more humid, which matched up with behaviors of other reported water-mediating proton conductors. Additionally, Hysteretic effects were also observed during measurements and the gaps between forward and backward sweep became larger as RH increased which can be indirect evidence for existence of ionic charge transport in addition to electronic conduction. We, therefore, performed EIS which has been considered as an appropriate method for the materials having ionic conductivity or high resistance. As the tool for characterizing frequency response of the

materials, it allows to the separation of the conductance of electrons and of ion. To measure impedance behavior of samples, alternating current (AC) was applied to the hybrid film and obtained information was represented in complex-impedance-plane called Nyquist plot (Figure 2.11). In case of the hybrid films, the measured Nyquist plots showed a semicircle and a tail with an angle of 45 degrees and it is typical shape of the impedance model for equivalent circuits proposed Randle consisting of charge transfer resistance (R_{ct}) and Warburg element. The presented semicircle curve at high frequencies in the complex plane manifested bulk resistance of the materials and the inclined lines at low frequency corresponds to impedance arising from the diffusion process of ions into electrode at surface of film/electrode. With values of bulk resistance taken from intersection of diameter in Nyquist plot we can calculated the conductivity of the films. As shown in Figure 2.12, the hybrid films exhibited a marked increase in their conductivity as RH increase and the conductivity reached 1.86 ($\pm$0.20) $\times$ 10^{-2} S/cm at 90 %RH at 25 °C, which is a considerably high value in comparison with other reported values of synthesized proton-conducting materials and bio material so far (Figure 2.13).

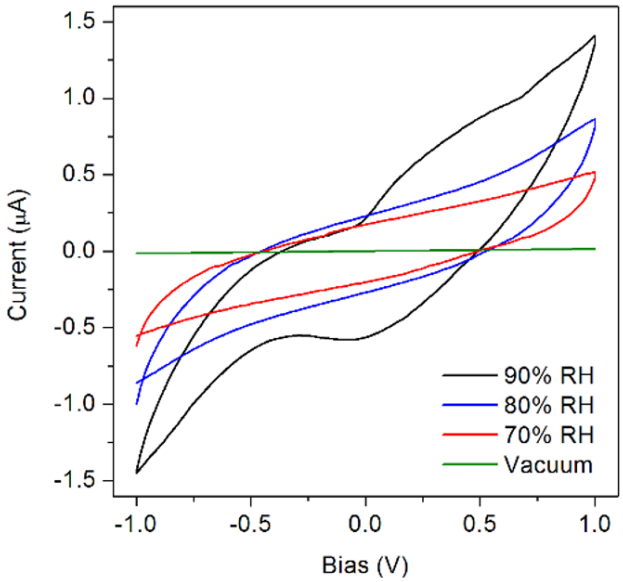

Figure 2.10 IV sweep plots (current versus voltage) of a peptide/manganese oxide hybrid film with gold contacts as a function of humidity. The device had a length of 10 μm, a width of 10 mm and a thickness of 130 nm.

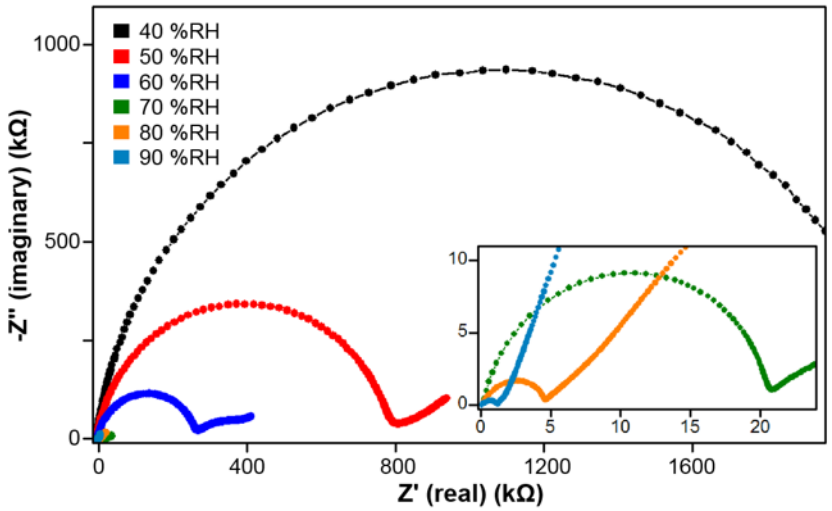

Figure 2.11 Typical Nyquist plots of the imaginary part of the impedance (Z'') versus the real part of the impedance (Z') by relative humidity for a gold electrode two-terminal device fabricated from peptide/manganese oxide hybrid material.

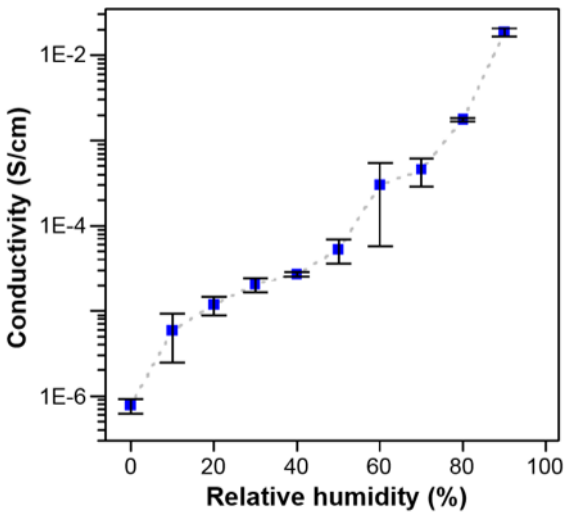

Figure 2.12 Calculated conductivity of the devices based on Nyquist plots by relative humidity.

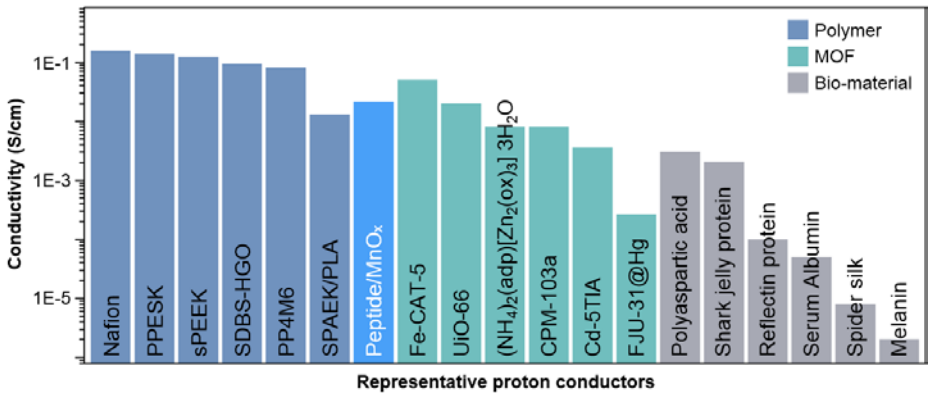

Figure 2.13 Comparison chart about proton conductivity with the other representative proton conducting materials at room temperature.

2.3.2 Deuterium kinetic isotope effect on conductivity of the hybrid films

Deuterium kinetic isotope effect on conductivity of the hybrid films was explored for better understanding towards the origin of conduction and it confirmed the charge carriers of the material was protons (or deuterons). The H/D isotope effect was screened from 10 %RH to 90 %RH as providing humidified inert gas by H_2O or D_2O and the results showed deuterium oxide made hybrid films less conductive (Figure 2.14). These comparison confirmed that increase in ionic contribution to electrical current by humidifying was originated from proton, whose migration was affected by water, mediating species making proton-conducting channel.

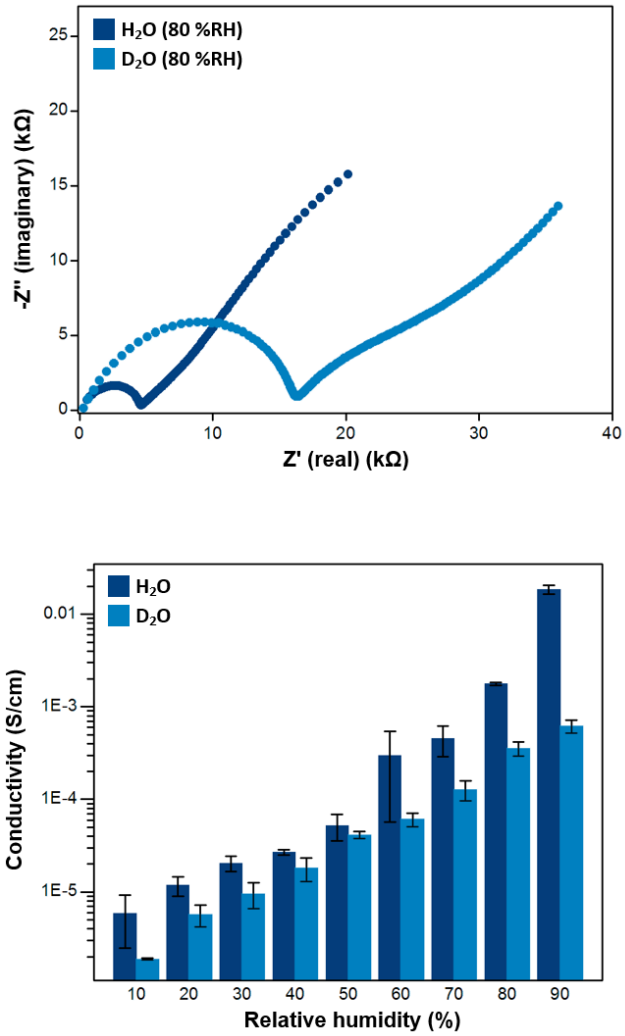

Figure 2.14 Nyquist plots in the presence of water vapor or deuterium oxide vapor (RH of 80%) and the calculated conductivity based on Nyquist plots by the relative humidity in presence of H_2O or D_2O vapor.

2.3.3 Transient current measurements for defining charge carriers

Transient current measurements were carried out to define the charge carrier of the material. The measurements were performed in two-terminal devices of hybrid films with Palladium (Pd) contacts and the current was recorded by applying constant 150 mV bias for 5 minutes and turning off the bias for another 5 minutes sequentially (Figure 2.15). At 80% RH, as providing the bias the films showed initial current of 180 nA and huge decrease in current arose immediately. Then only 3 % of initial current was maintained after 20 seconds. Because palladium is a metal having properties of electron conducting but ion blocking, it was inferred that this behavior of current drop would be originated from accumulation of proton at the electrode. It was supported by existence of reverse recovery current when the constant bias was suddenly reduced to zero at the steady state, which correlated with diffusion of accumulated charge carrier. Unlike these results from high degree of hydration, at the vacuum, only small constant current of 250 pA was obtained with applied bias and no reverse current was observed after removing bias. Therefore, it indicated that majority carrier of films in waterless condition didn't piled-up at metal electrode and allowed to think measured current at vacuum came from electron which get through the electrode without accumulation. These results with proton blocking electrode confirm that a large amount of current was attributed to migration of proton.

To decouple contribution of protonic current from mixed electrical properties of peptide/MnOx hybrid film, proton-transparent palladium hydride (PdH_x) electrode was hired and extent of proton contribution was estimated from steady state current in transient measurements. PdH_x electrodes has been considered as suitable metal for measuring protonic current with their ability to inject and release of proton, instead of the conventional proton-blocking metal forming space charge that results significant hysteresis in capacitance and resistance. According to an electrochemical reaction, $PdH_x \rightleftharpoons Pd + H^+ + e^-$, the hydrogenated palladium facilitates a quantification of protonic movement by completing the circuit for injected proton with involved electron of the reaction. Upon exposure to 5% H_2 balanced Ar gas on the devices fabricated with Pd contacts, PdH_x electrodes were prepared via absorption of hydrogen on the pristine metal. After conversion into PdH_x contacts, we measured the steady state current of the devices at 90 %RH and we founded its enhancement by a factor of fifty times than that of the devices with gold contacts at same RH (Figure 2.16). Furthermore, it was also observed that the extent of the steady state current got raised with higher degree of hydration, which was corresponded to typical tendency of proton-conducting biomolecules, and accounted up to 70% of the initial current (Figure 2.17).

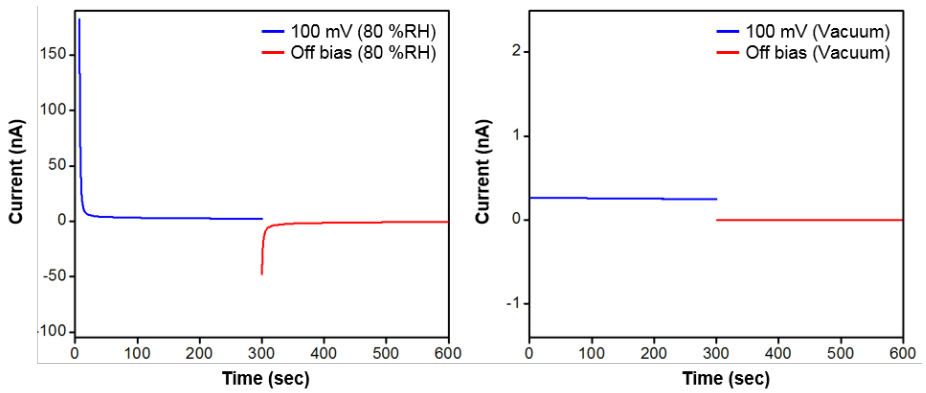

Figure 2.15 Comparison for the devices fabricated from peptide/manganese oxide hybrid material. The current were recorded with constant 100 mV bias for 300 seconds and another 300 seconds with no bias.

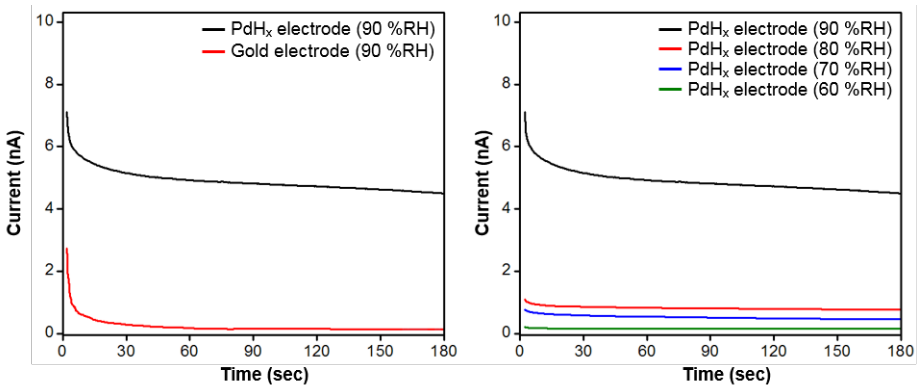

Figure 2.16 Transient current measurement of the devices with gold and palladium hydride electrode (left). Recorded current as function of relative humidity with PdH_x electrode (right). The current were recorded with constant 100 mV bias for 180 seconds.

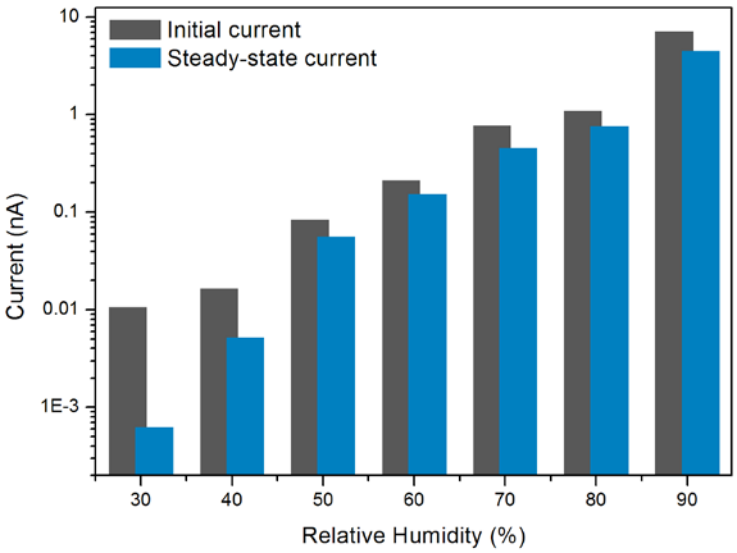

Figure 2.17 Recorded initial current and steady-state current as function of relative humidity with PdH_x electrode.

2.3.4 Investigation about the roles of each component in hybrid films

For understanding how the peptide and manganese species interrelate when the conduction occurs in the hybrid films, the roles of each component were investigated. To explore the role of MnO_x in the film, we controlled the concentration of $KMnO_4$ solution and treatment time of hybridization process. As a results, it was observed that higher concentration of the reactant solution and longer dipping time made the film thicker after the treatment (Figure 2.18), which implied that more manganese species were involved in the reactions. Then, conductivity of the device with these film were measured with EIS and calculated values were plotted as a function of RH (Figure 2.19). The results showed gradual decrease in conductivity at all RH (vacuum, 50 %RH, 90%RH) with more deposition of MnO_x and variation in amount of change between conductivity as humidity increased were very small to consider as noticeable change. These tendency suggested the role of manganese species might relate to electronic conduction of the film and it was supported by the results of the film without peptide. As preparation of the devices, the hybrid films was annealed at 400 °C that was set from thermal gravimetric analysis (TGA) of the film (Figure 2.20), so that it was a high temperature enough to decompose organic components while allowing to remain MnO_x without entailing an significant change in phase. In comparison with the results of original state, it was founded that the devices of baked films lost their hydration dependence of

the conductivity (Figure 2.21). These were clear evidences showing importance of peptide in proton transferring whereas MnO_x were more in charge of electronic conduction in the hybrid film.

We proceeded to further investigation about the peptide by altering the sequence of peptide film from YYACAYY to one having less tyrosine, YFACAFY and FFACAFF to gain insight about effect of tyrosine on proton conduction. During the bias was applied into the device from -1.0 V to +1.0 V, the current were recorded under the condition at 80 %RH and results were plotted in Figure 2.22. In I-V plots, it was founded that the only small current was observed in YFACAFY hybrid films. Calculated conductivity of two devices through EIS measurements showed differences in the conductivity level more clearly (Figure 2.23). In the results, the conductivity of YFACAFY hybrid films was smaller 85 times than that of YYACAYY hybrid films, which also suggested that tyrosine had a significant role in mediating protons in hybrid films.

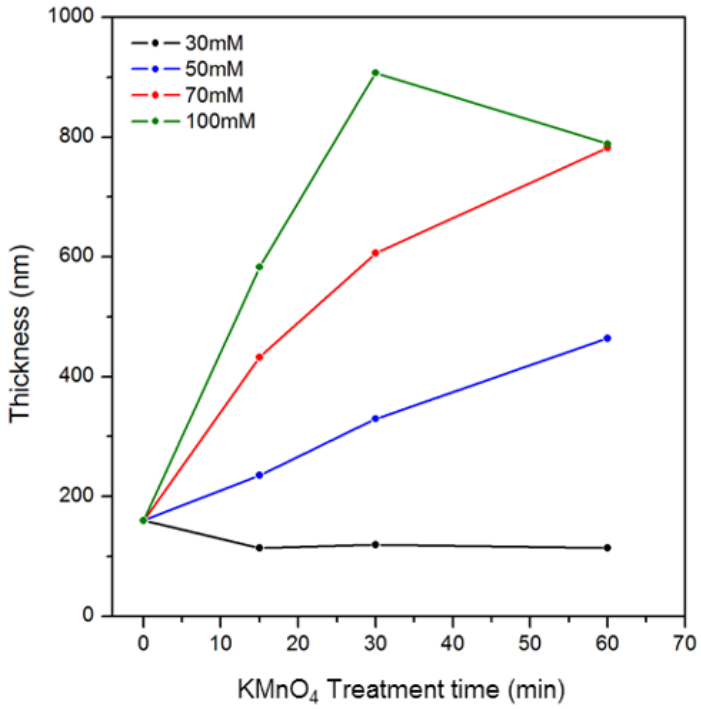

Figure 2.18 Thickness of pristine peptide films and hybrid films of various concentration of $KMnO_4$ solution by treatment time.

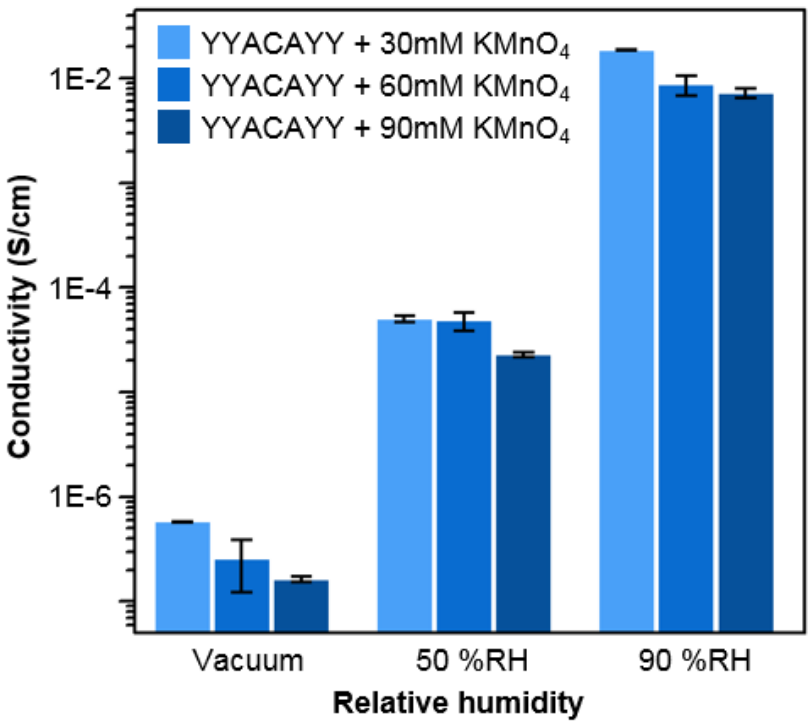

Figure 2.19 Conductivity of hybrid films treated with various concentration of $KMnO_4$ solution were calculated as a function of humidity through EIS measurements.

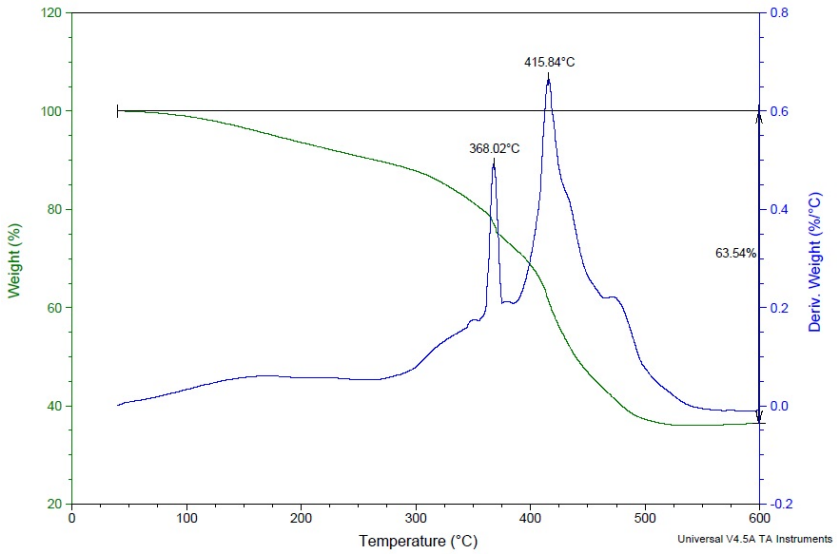

Figure 2.20 Result of TGA for peptide/Manganese oxide

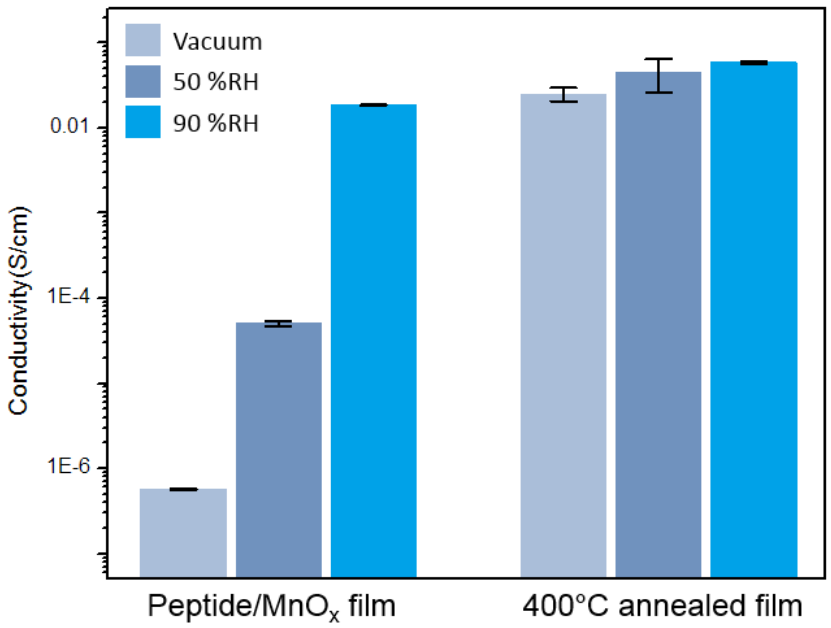

Figure 2.21 Calculated conductivity of hybrid film and high temperature annealed films through EIS measurements as a function of humidity.

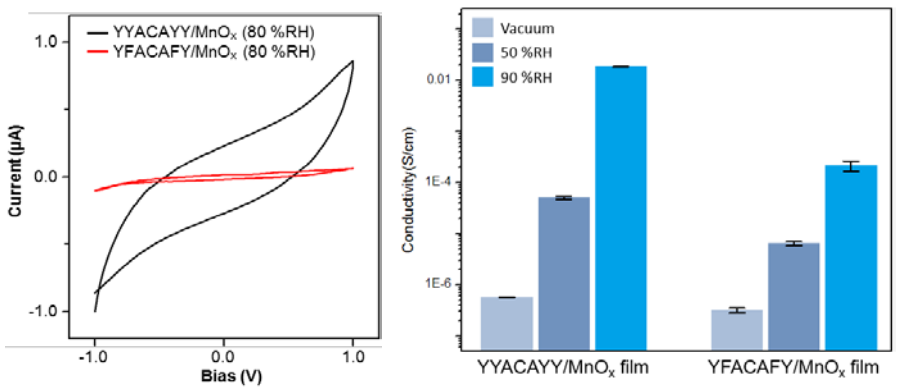

Figure 2.22 IV sweep plots of hybrid films from YYACAYY (black) and YFACAFY (red) peptides at 80 %RH. Calculated conductivity of hybrid films from YYACAYY or YFACAFY peptides through EIS measurements as a function of humidity

Chapter 3. Conclusion

Until now, β-sheet motifs were widely chosen to build 2D nanostructures.[52-56] However, macroscopic flatness of assembled structure with sheet arrangement is constrained by propeller-like twist in the shape of each β-strand, which is originated from structural factors such as chirality.[20,57] Interestingly, in peptide mimetic peptoid polymers, it was discovered that newly identified Σ-strand folding enables the atomically flat 2D assembly. In this context, our study can provide a valuable experimental evidence that emphasizes the importance of stabilization of helix for the further 2D and 3D assembly. Recently, it was also found that single heptad peptides can assemble into superhelical nanostructures by stabilizing helical conformation.[58]

In this study provides, to the best of our knowledge, the first demonstration of the 2D self-assembly behaviors of a pentapeptide on the surface of a water droplet. Interestingly, the dimerization process changes the morphology of the assembled structures from fibrils to giant sheets and also accelerates the facet formation kinetics at the air/water interface. The disulfide bond between the monomers stabilizes the helical conformation, resulting in strong molecular interactions and reinforced mechanical strength of the assembled structure. Our results provide new insight into the effect of short peptide folding on macroscale self-assembly. In addition, we open a new avenue of self-

assembling helical peptides that can construct transferable and giant 2D architectures with minimal molecular element.

Previously, we showed that YYACAYY sequence can assembled into giant nanosheets and suggested the potential of the peptide film as the robust 2-dimensional material with redox active functions. Along with it, inspired from nature, we made a new proton conducting material with tyrosine containing 2D peptide films by hybridization with inorganic species. In this process, our attempt also shows that functionalization of 2D peptide films and surface engineering can be done through a simple secondary treatment. In perspective of bioelectronics and further applications, it suggests one of good way for designing versatile bio-functionalized platforms with biocompatible materials. This exploration of peptide-based hybrid films as novel proton conductors has not been documented and remained significant implications to the both of biology and technology.

Experimental section

Chemicals. All peptides (98 % purity) were purchased from GL Biochem (Shanghai, China) and used without further purifications. Other solvents were purchased from Sigma-Aldrich.

Peptide Dimerization and Facet Formation. The monomer peptide was dissolved in deionized water and its concentration was 2 mM. After the solutions in 2 ml Eppendorf tubes rendered uniformly by tip sonicating for 2 min, they was placed in a heat block at 80 °C for air oxidation. After incubation for hours the disulfide bonding are formed from sulfhydryl residues of cysteine in monomer peptides. No faceting phenomenon was observed with samples incubating time of less than 20 hours. After an extracted aliquot (80 μL) from the enough oxidized solution was dropped on siliconized glass, faceting started within a few minutes. The average diameter of droplet was 6.4 mm.

Atomic Force Microscopy. 2 mM solutions of monomer peptides were incubated in 80 °C for air oxidation. After 4 days of incubation, an 80 μL of the solution was used for making an air/water interface film. The droplet was placed on siliconized glass for over 30 min to form a larger planar part of the peptide film. As enough time passed, film at the top part of the droplet was broken with a tweezer. Right after then surface was carefully transferred to SiO_2 coated silicon wafer (1 cm x 1 cm). This sample was immersed slowly in deionized water for washing out aggregations, and remained water on the film was removed by flowing N_2 gas gently with blower. Images of large area were observed from optical microscope (Axio Imager, Carl Zeiss, Germany) at various magnification. AFM analysis were carried out with Bruker AFM

multimode 8. The used probes for AFM were Antimony doped (n) silicon cantilevers with a spring constant of 40 Nm^{-1} (Bruker) and the resonance frequency of 300 kHz. The observation condition was tapping mode and a scan rate was 0.9 Hz. After acquiring AFM images, the thickness of film analyzed with the NanoScope Analysis program.

High Performance Liquid Chromatography. For measuring a conversion degree of dimer by oxidation time, a high performance liquid chromatography (HPLC) was performed by various aging time. After preparing 2mM monomeric peptide solutions, they was placed in the 80 °C heat block. An aliquot (500 μL) of the solution was extracted every 20 hours since an oxidizing reaction started. The extracted solution was dried up by lyophilization. An instrument for chromatographic separation was HP Agilent 1100 Series (Agilent Technologies, Germany) and the experiments was carried on SunFire C-18 analytical column (100 Å, 4.6 x 250 mm, 5 μm, Waters, Milford, MA) with steady changes of the mobile phase composition during the run. Started with 90 % water and 10 % acetonitrile containing 0.1 % trifluoroacetic acid, the eluent mixing gradient linearly changed to 100 % acetonitrile in 30 minutes. The mixed eluent pumped at a flow rate of 1 mL/min. For injection, lyophilized samples dissolved in pure methanol (2mM) and injection volume was 20 μL. The retention times of monomeric and dimerized peptide were about 13.3 and 14.3 min respectively.

Electrospray Ionization (ESI) Mass Spectrometer. The monomeric peptide and 4 days air oxidized peptide (2 mM, lyophilized) was dissolved in pure methanol. Equipped with autosampler and PDA-UV detector, a Thermo-Finnigan Surveyor (Thermo Scientific, USA) and ThermoFinnigan LCQ Deca XP plus ion trap mass spectrometer with ESI interface were used for the mass

analysis. Ionization of analytes was carried out using electrospray ionization at 275°C of capillary temperature. The capillary voltage was set at 45 V in positive mode and -15 V in negative ionization mode with 5kV of ion source voltage. The sheath and Aux gas was set at 30 and 5units. The average scan time was 0.01 min while the average time to change polarity was 0.02 min. In order to maintain 35% abundance of the precursor ion, the collision energy (CE) level was set general value.

***Raman Spectroscopy*.** Raman data were measured by Horiba Jobin-Yvon LabRam Aramis Raman spectrometer. A 785 nm Ar-ion laser was used as the excitation source and substrate plate was stainless steel which had no Ramam signal and guaranteed a free fluorescence background. Wave numbers ranged from 200 cm^{-1} to 3000 cm^{-1} was scanned and each spectrum was accumulated for 60 seconds. The analysis was executed more than 3 points in each sample for reproducibility and reliability. To get the data of peptide film, it was transferred to the substrate and just single transfer of film provided enough signals for interpreting the Raman peaks.

***Circular Dichroism Spectroscopy*.** Circular dichroism spectra of peptide solutions and peptide films were measured with J-815 spectropolarimeter (Jasco, Tokyo, Japan) at 25 °C. Spectra were collected from 260 nm to 180 nm by using a 0.1 cm path length quartz cuvette during keeping HT voltage less than 500 V for reliability. The experiment conditions were a 0.5 nm data pitch, a 20 nm/min scan speed, 16 sec response time and a 1 nm bandwidth. The data were accumulated from 3 repeated runs for reproducibility and smoothing process was done. In order to acquire conformational information of peptide films, solid circular dichroism was carried with same conditions. After faceting

of a droplet was almost saturated, peptide films were transferred to quartz cuvette surface and rinsed with deionized water.

Two-dimensional Nuclear Magnetic Resonance Spectroscopy. All NMR spectra were measured at 298K on Agilent DD2 600 MHz spectrometer at Korea Institute of Science and Technology. Dimethylsulfoxide (DMSO) was used to detect the gamma protons of cysteine. DMSO can also oxidize cysteines to form a disulfide bridge.[62] The 3 mM of YFCFY peptide dissolved in 100% DMSO-d6 was used for NMR experiments. For the assignments of amide and alpha protons, identification of sequential connectivity, and the secondary structure prediction of YFCFY, 2D COSY, 2D TOCSY, and 2D NOESY experiments were performed. For TOCSY, an MLEV-17 spinlock pulse with a mixing time of 80 ms was used. For NOESY, the mixing times of 200 and 450 ms were used.[63-65] All NMR spectra were processed with VnmrJ3.2 (Agilent Technologies, Inc.) and NMRpipe[66] and visualized with Sparky software[67].

Scanning Electron Microscopy. The micrographs were obtained using a Zeiss Supra 55 VP instrument operating at 2 kV. The samples were prepared by dropping colloidal solutions onto silicon wafers.

Transmission Electron Microscopy. The micrographs and selected area electron diffraction (SAED) patterns were obtained using a JEOL JEM-3000F FEG TEM instrument with an acceleration voltage of 200 kV.

UV-Visible Spectroscopy. The spectra were taken using a Thermo Scientifc NanoDrop 2000c UV/Vis Spectrophotometer in the 180-800 nm wavelength.

X-ray Absorption Near Edge Structure. The oxidation state corresponding to

the Mn K-edge in each sample was investigated using XANES analysis. In-situ XANES spectra were collected in fluorescence mode with an electron energy of 2.5 GeV and stored in the current of 250mA top-up mode.

Photoluminescence Spectroscopy. Emission spectra were recorded on a PTI QuantaMaster™ 400 spectrofluorometer. The spectra were collected by titrating 500 μM $KMnO_4$ solution (DI) 20 μL into 2 μM peptide solution (HFIP) in cuvette (3 ml). The original system (peptide 17 mM : KMnO4 30mM) was considered and the final ratio was 2 μM peptide and 3.3 μM $KMnO_4$.

Inductively Coupled Plasma - Mass Spectroscopy. Analysis was carried ourt with NexION 350D and Perkin-Elmer SCIEX. The source was argon plasma (6000K) and the range of mass resolution was 0.3-3.0 amu. Its detection limit was 9Be<15ppt, 59 Co<2ppt, 115In<0.5ppt. RF Power was 1100W and injection was performed with flow rate of 1.00 ml/min.

Electrochemical Impedance Spectroscopy. For two terminal AC measurements on quartz substrates, the impedance data were recorded an Agilent 4294A Impedance Analyzer. The humidity was monitored constantly with a hygrometer during all experiments.

Thermal Gravimetric Analysis. Thermo gravimetric measurements were performed with a Q 5000 IR TGA instrument (TA Instruments). High-temperature platinum pans loaded with 15 mg samples were used for the tests. All samples, previously dried to remove the adsorbed water, was heated from room temperature to 400 °C with a heating rate of 5 °C min^{-1}, using nitrogen as purge gas (10 ml min^{-1}).

References

1. Lee, J.-H.; Lee, J. H.; Lee, Y. J.; Nam, K. T. Protein/peptide Based Nanomaterials for Energy Application. *Curr. Opin. Biotechnol.* 2013, *24*, 599–605.
2. Kim, S.; Kim, J. H.; Lee, J. S.; Park, C. B. Beta-Sheet-Forming, Self-Assembled Peptide Nanomaterials towards Optical, Energy, and Healthcare Applications. *Small* 2015, *11*, 3623–3640.
3. Crookes-Goodson, W. J.; Slocik, J. M.; Naik, R. R. Bio-Directed Synthesis and Assembly of Nanomaterials. *Chem. Soc. Rev.* 2008, *37*, 2403–2412.
4. Hauser, C. A. E.; Deng, R.; Mishra, A.; Loo, Y.; Khoe, U.; Zhuang, F.; Cheong, D. W.; Accardo, A.; Sullivan, M. B.; Riekel, C.; *et al.* Natural Tri- to Hexapeptides Self-Assemble in Water to Amyloid β-Type Fiber Aggregates by Unexpected α-Helical Intermediate Structures. *Proc. Natl. Acad. Sci.* 2011, *108*, 1361–1366.
5. Sarkar, B.; O'Leary, L. E. R.; Hartgerink, J. D. Self-Assembly of Fiber-Forming Collagen Mimetic Peptides Controlled by Triple-Helical Nucleation. *J. Am. Chem. Soc.* 2014, *136*, 14417–14424.
6. Li, Q.; Jia, Y.; Dai, L.; Yang, Y.; Li, J. Controlled Rod Nanostructured Assembly of Diphenylalanine and Their Optical Waveguide Properties. *ACS Nano* 2015, *9*, 2689–2695.
7. Hamley, I. W.; Dehsorkhi, A.; Castelletto, V.; Seitsonen, J.; Ruokolainen, J.; Iatrou, H. Self-Assembly of a Model Amphiphilic Oligopeptide Incorporating an Arginine Headgroup. *Soft Matter* 2013, *9*, 4794.

8. Mason, T. O.; Chirgadze, D. Y.; Levin, A.; Adler-Abramovich, L.; Gazit, E.; Knowles, T. P. J.; Buell, A. K. Expanding the Solvent Chemical Space for Self-Assembly of Dipeptide Nanostructures. *ACS Nano* 2014, *8*, 1243–1253.
9. Sun, L.; Fan, Z.; Wang, Y.; Huang, Y.; Schmidt, M.; Zhang, M. Tunable Synthesis of Self-Assembled Cyclic Peptide Nanotubes and Nanoparticles. *Soft Matter* 2015, *11*, 3822–3832.
10. Rubin, D. J.; Amini, S.; Zhou, F,; Su, H,; Miserez, A.; Joshi, N.S. Structural, Nanomechanical, and Computational Characterization of D,L-Cyclic Peptide Assemblies. *ACS Nano* 2015, 9, 3360–3368.
11. Hamley, I. W. Peptide Nanotubes. *Angew. Chemie. Int. Ed.* 2014, *53*, 6866–6881.
12. Lim, Y. B.; Lee, E.; Lee, M. Cell-Penetrating-Peptide-Coated Nanoribbons for Intracellular Nanocarriers. *Angew. Chem. Int. Ed.* 2007, *46*, 3475–3478.
13. Uesaka, A.; Ueda, M.; Makino, A.; Imai, T.; Sugiyama, J.; Kimura, S. Morphology Control between Twisted Ribbon, Helical Ribbon, and Nanotube Self-Assemblies with His-Containing Helical Peptides in Response to pH Change. *Langmuir* 2014, *30*, 1022–1028.
14. Mondal, J. H.; Ahmed, S.; Ghosh, T.; Das, D. Reversible Deformation–Formation of a Multistimuli Responsive Vesicle by a Supramolecular Peptide Amphiphile. *Soft Matter* 2015, *11*, 4912–4920.
15. Black, M.; Trent, A.; Kostenko, Y.; Lee, J. S.; Olive, C.; Tirrell, M. Self-Assembled Peptide Amphiphile Micelles Containing a Cytotoxic T-Cell Epitope Promote a Protective Immune Response In Vivo. *Adv. Mater.* 2012, *24*, 3845–3849.

16. Rad-Malekshahi, M.; Visscher, K. M.; Rodrigues, J. P. G. L. M.; de Vries, R.; Hennink, W. E.; Baldus, M.; Bonvin, A. M. J. J.; Mastrobattista, E.; Weingarth, M. The Supramolecular Organization of a Peptide-Based Nanocarrier at High Molecular Detail. *J. Am. Chem. Soc.* 2015, *137*, 7775–7784.

17. Dai, B.; Li, D.; Xi, W.; Luo, F.; Zhang, X.; Zou, M.; Cao, M.; Hu, J.; Wang, W.; Wei, G.; *et al.* Tunable Assembly of Amyloid-Forming Peptides into Nanosheets as a Retrovirus Carrier. *Proc. Natl. Acad. Sci.* 2015, *112*, 2996–3001.

18. Pellach, M.; Atsmon-Raz, Y.; Simonovsky, E.; Gottlieb, H.; Jacoby, G.; Beck, R.; Adler-Abramovich, L.; Miller, Y.; Gazit, E. Spontaneous Structural Transition in Phospholipid-Inspired Aromatic Phosphopeptide Nanostructures. *ACS Nano* 2015, *9*, 4085–4095.

19. Segman-Magidovich, S.; Lee, M.; Vaiser, V.; Struth, B.; Gellman, S. H.; Rapaport, H. Sheet-Like Assemblies of Charged Amphiphilic α/β-Peptides at the Air-Water Interface. *Chem. - A Eur. J.* 2011, *17*, 14857–14866.

20. Nam, K. T.; Shelby, S. a; Choi, P. H.; Marciel, A. B.; Chen, R.; Tan, L.; Chu, T. K.; Mesch, R. a; Lee, B.-C.; Connolly, M. D.; *et al.* Free-Floating Ultrathin Two-Dimensional Crystals from Sequence-Specific Peptoid Polymers. *Nat. Mater.* 2010, *9*, 454–460.

21. Zhang, S.; Holmes, T.; Lockshin, C.; Rich, A. Spontaneous Assembly of a Self-Complementary Oligopeptide to Form a Stable Macroscopic Membrane. *Proc. Natl. Acad. Sci. U. S. A.* 1993, *90*, 3334–3338.

22. O'Leary, L. E. R.; Fallas, J. A.; Bakota, E. L.; Kang, M. K.;

Hartgerink, J. D. Multi-Hierarchical Self-Assembly of a Collagen Mimetic Peptide from Triple Helix to Nanofibre and Hydrogel. *Nat. Chem.* 2011, *3*, 821–828.

23. Chopko, C. C. M.; Lowden, E. E. L.; Engler, A. A. C.; Griffith; Hammond; Griffith, L. G.; Hammond, P. T.; Paula, T. Dual Responsiveness of a Tunable Thermo-Sensitive Polypeptide. *ACS Macro Lett.* 2012, *1*, 727–731.
24. Raspa, A.; Saracino, G. a. a.; Pugliese, R.; Silva, D.; Cigognini, D.; Vescovi, A.; Gelain, F. Complementary Co-Assembling Peptides: From In Silico Studies to In Vivo Application. *Adv. Funct. Mater.* 2014, *24*, 6317–6328.
25. Zhuang, X.; Mai, Y.; Wu, D.; Zhang, F.; Feng, X. Two-Dimensional Soft Nanomaterials: A Fascinating World of Materials. *Adv. Mater.* 2015, *27*, 403–427.
26. Xue, T.; Peng, B.; Xue, M.; Zhong, X.; Chiu, C.-Y.; Yang, S.; Qu, Y.; Ruan, L.; Jiang, S.; Dubin, S.; *et al.* Integration of Molecular and Enzymatic Catalysts on Graphene for Biomimetic Generation of Antithrombotic Species. *Nat. Commun.* 2014, *5*, 1–6.
27. Tan, C.; Zhang, H. Wet-Chemical Synthesis and Applications of Non-Layer Structured Two-Dimensional Nanomaterials. *Nat Commun* 2015, *6*, 1–13.
28. Rao, C. N. R.; Sood, A. K.; Subrahmanyam, K. S.; Govindaraj, A. Graphene: The New Two-Dimensional Nanomaterial. *Angew. Chemie. Int. Ed.* 2009, *48*, 7752–7777.
29. Robertson, E. J.; Olivier, G. K.; Qian, M.; Proulx, C.; Zuckermann, R. N.; Richmond, G. L. Assembly and Molecular Order of Two-Dimensional Peptoid Nanosheets through the Oil–water Interface.

Proc. Natl. Acad. Sci. 2015, *112*, E338–E338.

30. Kory, M. J.; Wörle, M.; Weber, T.; Payamyar, P.; van de Poll, S. W.; Dshemuchadse, J.; Trapp, N.; Schlüter, A. D. Gram-Scale Synthesis of Two-Dimensional Polymer Crystals and Their Structure Analysis by X-Ray Diffraction. *Nat. Chem.* 2014, *6*, 779–784.
31. Musevic, I.; Skarobot, M.; Tkalec, U.; Ravnik, M.; Zumer, S. Two-Dimensional Nematic Colloidal Crystals Self-Assembled by Topological Defects. *Science* 2006, *313*, 954–958.
32. Kunitake, T. Synthetic Bilayer Membranes: Molecular Design, Self-Organization, and Application. *Angew. Chem. Int. Ed.* 1992, *31*, 709–726.
33. Knowles, T. P. J.; Oppenheim, T. W.; Buell, A. K.; Chirgadze, D. Y.; Welland, M. E. Nanostructured Films from Hierarchical Self-Assembly of Amyloidogenic Proteins. *Nat. Nanotechnol.* 2010, *5*, 204–207.
34. Jang, H.-S.; Lee, J.-H.; Park, Y.-S.; Kim, Y.-O.; Park, J.; Yang, T.-Y.; Jin, K.; Lee, J.; Park, S.; You, J. M.; *et al.* Tyrosine-Mediated Two-Dimensional Peptide Assembly and Its Role as a Bio-Inspired Catalytic Scaffold. *Nat. Commun.* 2014, *5*, 3665.
35. Kiefer, W. Recent Advances in Linear and Nonlinear Raman Spectroscopy I. *J. Raman Spectrosc.* 2007, *38*, 1538–1553.
36. Tuma, R. Raman Spectroscopy of Proteins: From Peptides to Large Assemblies. *J. Raman Spectrosc.* 2005, *36*, 307–319.
37. M. Siamwiza, R. Lord, M. Chen, Biochemistry 1975, 14, 4870–4876.
38. E. B. Wilson, Phys. Rev. 1934, 45, 706–714.
39. E. Podstawka, A. Kudelski, P. Kafarski, L. M. Proniewicz, Surf. Sci. 2007, 601, 4586–4597.

40. M. C. Chen, R. C. Lord, Biochemistry 1976, 15, 1889–1897.

41. C. N. Pace, G. Horn, E. J. Hebert, J. Bechert, K. Shaw, L. Urbanikova, J. M. Scholtz, J. Sevcik, J. Mol. Biol. 2001, 312, 393–404.

42. Beychok, S. Circular Dichroism of Biological Macromolecules. *Science* 1966, *154*, 1288–1299.

43. Goodman, M.; Toniolo, C.; Peggion, E. Conformational Aspects of Polypeptides. XXIX. Conformational Assignments for Some Aromatic Polypeptides by Far-UV Cotton Effects. New Results. *Biopolymers* 1968, *6*, 1691–1695.

44. Fretto, L.; Strickland, E. H. Effect of Temperature Upon the Conformations of Carboxypeptidase A (Anson), A_{γ}^{Leu}, A_{γ}^{Val}, and $A_{\alpha+\beta}$. *Biochim. Biophys. Acta (BBA)-Enzymology* 1971, *235*, 473–488.

45. Beychok, S.; Fasman, G. D. Circular Dichroism of Poly-L-Tyrosine*. *Biochemistry* 1964, *3*, 1675–1678.

46. Chen, Y. H.; Lo, T. B.; Yang, J. T. Optical Activity and Conformation of Cobra Neurotoxin. *Biochemistry* 1977, *16*, 1826–1830.

47. Cameron, D. L.; Tu, a T. Characterization of Myotoxin a from the Venom of Prairie Rattlesnake (Crotalus Viridis Viridis). *Biochemistry* 1977, *16*, 2546–2553.

48. Timasheff, S. N.; Bernardi, G. Studies on Acid Deoxyribonuclease: VII. Conformation of Three Nucleases in Solution. *Arch. Biochem. Biophys.* 1970, *141*, 53–58.

49. Polese, A.; Formaggio, F.; Crisma, M.; Valle, G.; Toniolo, C.; Bonora, G. M.; Broxterman, Q. B.; Kamphuis, J. Peptide Helices as

Rigid Molecular Rulers: A Conformational Study of Isotactic Homopeptides from α-Methyl-α-Isopropylglycine, [L-(αMe)Val]$_n$. *Chem. - A Eur. J.* 1996, *2*, 1104–1111.

50. Toniolo, C.; Polese, a; Formaggio, F.; Crisma, M.; Kamphuis, J. Circular Dichroism Spectrum of a Peptide 3_{10}-Helix. *J. Am. Chem. Soc.* 1996, *118*, 2744–2745.
51. Yoder, G.; Polese, A.; Silva, R. A. G. D.; Formaggio, F.; Crisma, M.; Broxterman, Q. B.; Kamphuis, J.; Toniolo, C.; Keiderling, T. A. Conformational Characterization of Terminally Blocked L -(αMe)Val Homopeptides Using Vibrational and Electronic Circular Dichroism. 3_{10}-Helical Stabilization by Peptide−Peptide Interaction. *J. Am. Chem. Soc.* 1997, *119*, 10278–10285.
52. Fasman, G. D. Poly-α-Amino Acids: Protein Models for Conformational Studies. Marcel Dekker: New York, 1967.
53. Kurapkat, G.; Krüger, P.; Wollmer, a; Fleischhauer, J.; Kramer, B.; Zobel, E.; Koslowski, a; Botterweck, H.; Woody, R. W. Calculations of the CD Spectrum of Bovine Pancreatic Ribonuclease. *Biopolymers* 1997, *41*, 267–287.
54. Goux, W. J.; Hooker, T. M. Chiroptical Properties of Proteins. 1. Near-Ultraviolet Circular Dichroism of Ribonuclease S. *J. Am. Chem. Soc.* 1980, *156*, 7080–7087.
55. Woody, R. W.; Dunker, A. K. Aromatic and Cystine Side-Chain Circular Dichroism in Proteins. *Circular Dichroism and the Conformational Analysis of Biomolecules*; Plenum Press: New York, 1996; pp. 109–157.
56. Wütrich, K. *NMR of Proteins and Nucleic Acids*, John Wiley & Sons: New York, 1986.

57. J. Cavanagh, W. J. Fairbrother, A. G. Palmer, M. Rance, N. J. Skelton, *Protein NMR Spectroscopy: Principles and Practice*, Elsevier Academic Press, 2nd Ed. 2007.

58. Zarbock, J.; Clore, G. M.; Gronenborn, a M. Nuclear-Magnetic-Resonance Study of the Globular Domain of Chicken Histone H-5 - Resonance Assignment and Secondary Structure. *Proc. Natl. Acad. Sci. U. S. A.* 1986, *83*, 7628–7632.

59. Bax, A. Two-Dimensional NMR and Protein Structure[1, 2]. *Annu. Rev. Biochem.* 1989, *58*, 223–256.

60. Rapaport, H.; Kjaer, K.; Jensen, T. R.; Leiserowitz, L.; Tirrell, D. a. Two-Dimensional Order in β-Sheet Peptide Monolayers. *J. Am. Chem. Soc.* 2000, *122*, 12523–12529.

61. Lamm, M. S.; Rajagopal, K.; Schneider, J. P.; Pochan, D. J. Laminated Morphology of Nontwisting β-Sheet Fibrils Constructed via Peptide Self-Assembly. *J. Am. Chem. Soc.* 2005, *127*, 16692–16700.

62. Benzinger, T. L.; Gregory, D. M.; Burkoth, T. S.; Miller-Auer, H.; Lynn, D. G.; Botto, R. E.; Meredith, S. C. Two-Dimensional Structure of β-amyloid(10-35) Fibrils. *Biochemistry* 2000, *39*, 3491–3499.

63. Hughes, M.; Xu, H.; Frederix, P. W. J. M.; Smith, A. M.; Hunt, N. T.; Tuttle, T.; Kinloch, I. A.; Ulijn, R. V. Biocatalytic Self-Assembly of 2D Peptide-Based Nanostructures. *Soft Matter* 2011, *7*, 10032–10038.

64. Aggeli, a; Fytas, G.; Vlassopoulos, D.; McLeish, T. C.; Mawer, P. J.; Boden, N. Structure and Dynamics of Self-Assembling β-Sheet Peptide Tapes by Dynamic Light Scattering. *Biomacromolecules*

2001, *2*, 378–388.

65. Mannige, R. V.; Haxton, T. K.; Proulx, C.; Robertson, E. J.; Battigelli, A.; Butterfoss, G. L.; Zuckermann, R. N.; Whitelam, S. Peptoid Nanosheets Exhibit a New Secondary-Structure Motif. *Nature* 2015, 2–9.
66. Mondal, S.; Adler-Abramovich, L.; Lampel, A.; Bram, Y.; Lipstman, S.; Gazit, E. Formation of Functional Super-Helical Assemblies by Constrained Single Heptad Repeat. *Nat. Commun.* 2015, *6*, 8615.
67. Tam, J. P.; Wu, C. R.; Liu, W.; Zhang, J. W. Disulfide Bond Formation in Peptides by Dimethyl-Sulfoxide - Scope and Applications. *J. Am. Chem. Soc.* 1991, *113*, 6657–6662.
68. Bax, A.; Davis, D. G. Practical Aspects of Two-Dimensional Transverse NOE Spectroscopy. *J. Magn. Reson.* 1985, 63, 207–213.
69. Bax, A.; Davis, D. G. MLEV-17-based Two-Dimensional Homonuclear Magnetization Transfer Spectroscopy. *J. Magn. Reson.* 1985, 65, 335–360.
70. Marion, D.; Wu¨thrich, K. Application of Phase Sensitive Two-Dimensional Correlated Spectroscopy (COSY) for Measurements of 1H–1H Spin–Spin Coupling Constants in Proteins. *Biochem. Biophys. Res. Commun.* 1983, 113, 967–974..
71. Delagio, F. et al. NMRPipe: a Multidimensional Spectral Processing System Based on UNIX Pipes. *J. Biomol. NMR* 1995, 6, 277–293.
72. Goddard, T. D.; Kneller, D. G. SPARKY 3, Univ. of California, 2002.
73. PANSINI, Angela, Ferruccio GUERRIERI, and Sergio PAPA. "Control of Proton Conduction by the H+-ATPase in the Inner Mitochondrial Membrane." *European Journal of Biochemistry* 92.2 (1978): 545-551.

74. Lozier, RICHARD H., ROBERTO A. Bogomolni, and W. Stoeckenius. "Bacteriorhodopsin: a light-driven proton pump in Halobacterium Halobium." *Biophysical journal* 15.9 (1975): 955.
75. Tombola, Francesco, Maximilian H. Ulbrich, and Ehud Y. Isacoff. "The voltage-gated proton channel Hv1 has two pores, each controlled by one voltage sensor." *Neuron* 58.4 (2008): 546-556.
76. Pomes, Regis, and Benoît Roux. "Theoretical study of H+ translocation along a model proton wire." *The Journal of Physical Chemistry* 100.7 (1996): 2519-2527.
77. Hirst, Judy, et al. "Kinetics and mechanism of redox-coupled, long-range proton transfer in an iron-sulfur protein. Investigation by fast-scan protein-film voltammetry." *Journal of the American Chemical Society* 120.28 (1998): 7085-7094.
78. Meyer, Thomas J., My Hang V. Huynh, and H. Holden Thorp. "The Possible Role of Proton-Coupled Electron Transfer (PCET) in Water Oxidation by Photosystem II." *Angewandte Chemie International Edition* 46.28 (2007): 5284-5304.
79. Huynh, My Hang V., and Thomas J. Meyer. "Proton-coupled electron transfer." *Chemical Reviews* 107.11 (2007): 5004-5064.
80. Reichard, Peter, and Anders Ehrenberg. "Ribonucleotide reductase--a radical enzyme." *Science* 221.4610 (1983): 514-519.
81. Hammarström, Leif, and Stenbjörn Styring. "Proton-coupled electron transfer of tyrosines in Photosystem II and model systems for artificial photosynthesis: the role of a redox-active link between catalyst and photosensitizer." *Energy & Environmental Science* 4.7 (2011): 2379-2388.
82. Bleifuss, Günther, et al. "Tryptophan and tyrosine radicals in

ribonucleotide reductase: a comparative high-field EPR study at 94 GHz." *Biochemistry* 40.50 (2001): 15362-15368.

83. Moser, Christopher C., et al. "Nature of biological electron transfer." *Nature*355.6363 (1992): 796-802.

84. Sazanov, Leonid A. "A giant molecular proton pump: structure and mechanism of respiratory complex I." *Nature Reviews Molecular Cell Biology* 16.6 (2015): 375-388.

85. Croce, Roberta, and Herbert Van Amerongen. "Natural strategies for photosynthetic light harvesting." *Nature chemical biology* 10.7 (2014): 492-501.

86. Kreuer, Klaus-Dieter. "Proton conductivity: materials and applications." *Chemistry of Materials* 8.3 (1996): 610-641.

87. Athens, George L., Yair Ein-Eli, and Bradley F. Chmelka. "Acid-Functionalized Mesostructured Aluminosilica for Hydrophilic Proton Conduction Membranes." *Advanced Materials* 19.18 (2007): 2580-2587.

88. Ōkawa, Hisashi, et al. "Proton-Conductive Magnetic Metal–Organic Frameworks,{NR3 (CH2COOH)}[MaIIMbIII (ox) 3]: Effect of Carboxyl Residue upon Proton Conduction." *Journal of the American Chemical Society* 135.6 (2013): 2256-2262.

89. Sel, Ozlem, et al. "Sulfonic and phosphonic acid and bifunctional organic–inorganic hybrid membranes and their proton conduction properties." *Chemistry–An Asian Journal* 6.11 (2011): 2992-3000.

90. Ordinario, David D., et al. "Bulk protonic conductivity in a cephalopod structural protein." *Nature chemistry* 6.7 (2014): 596-602.

91. Josberger, Erik E., et al. "Proton conductivity in ampullae of

Lorenzini jelly." *Science Advances* 2.5 (2016): e1600112.

92. Mostert, Albertus B., et al. "Role of semiconductivity and ion transport in the electrical conduction of melanin." *Proceedings of the National Academy of Sciences* 109.23 (2012): 8943-8947.
93. Wünsche, Julia, et al. "Protonic and electronic transport in hydrated thin films of the pigment eumelanin." *Chemistry of Materials* 27.2 (2015): 436-442.
94. Kreuer, K. D. "On the development of proton conducting materials for technological applications." *Solid state ionics* 97.1 (1997): 1-15.
95. Kreuer, K. D. "Proton-conducting oxides." *Annual Review of Materials Research* 33.1 (2003): 333-359.
96. Iwahara, Hiroyasu. "Proton conducting ceramics and their applications." *Solid State Ionics* 86 (1996): 9-15.
97. Yajima, T., et al. "Proton conduction in sintered oxides based on CaZrO3." *Solid State Ionics* 47.3-4 (1991): 271-275.
98. Norby, Truls, and Yngve Larring. "Concentration and transport of protons in oxides." *Current Opinion in Solid State and Materials Science* 2.5 (1997): 593-599.
99. Norby, Truls. "Solid-state protonic conductors: principles, properties, progress and prospects." *Solid State Ionics* 125.1 (1999): 1-11.
100. Minh, Nguyen Q. "Ceramic fuel cells." *Journal of the American Ceramic Society* 76.3 (1993): 563-588.
101. Boysen, Dane A., et al. "High-performance solid acid fuel cells through humidity stabilization." *Science* 303.5654 (2004): 68-70.
102. Haile, Sossina M., et al. "Solid acid proton conductors: from laboratory curiosities to fuel cell electrolytes." *Faraday*

discussions 134 (2007): 17-39.

103. Nakamura, Osamu, et al. "High-conductivity solid proton conductors: dodecamolybdophosphoric acid and dodecatungstophosphoric acid crystals." *Chemistry Letters* 8.1 (1979): 17-18.
104. Uda, Tetsuya, and Sossina M. Haile. "Thin-membrane solid-acid fuel cell." *Electrochemical and Solid-State Letters* 8.5 (2005): A245-A246.
105. Xu, Gang, et al. "Superprotonic Conductivity in a Highly Oriented Crystalline Metal–Organic Framework Nanofilm." *Journal of the American Chemical Society* 135.20 (2013): 7438-7441.
106. Liang, Xiaoqiang, et al. "From metal–organic framework (MOF) to MOF–polymer composite membrane: enhancement of low-humidity proton conductivity." *Chemical Science* 4.3 (2013): 983-992.
107. Shimizu, George KH, Jared M. Taylor, and SiRim Kim. "Proton conduction with metal-organic frameworks." *Science* 341.6144 (2013): 354-355.
108. Sen, Susan, et al. "High proton conductivity by a metal–organic framework incorporating Zn8O clusters with aligned imidazolium groups decorating the channels." *Journal of the American Chemical Society* 134.47 (2012): 19432-19437.
109. Sadakiyo, Masaaki, Teppei Yamada, and Hiroshi Kitagawa. "Rational designs for highly proton-conductive metal− organic frameworks." *Journal of the American Chemical Society* 131.29 (2009): 9906-9907.
110. Kreuer, K. D. "On the development of proton conducting polymer

membranes for hydrogen and methanol fuel cells." Journal of membrane science 185.1 (2001): 29-39.

111. Carretta, N., V. Tricoli, and F. Picchioni. "Ionomeric membranes based on partially sulfonated poly (styrene): synthesis, proton conduction and methanol permeation." *Journal of Membrane Science* 166.2 (2000): 189-197.
112. Paddison, S. J. "Proton conduction mechanisms at low degrees of hydration in sulfonic acid-based polymer electrolyte membranes." *Annual Review of Materials Research* 33.1 (2003): 289-319.
113. Alberti, G., et al. "Polymeric proton conducting membranes for medium temperature fuel cells (110–160 C)." *Journal of Membrane Science* 185.1 (2001): 73-81.
114. Sumner, J. J., et al. "Proton conductivity in Nafion® 117 and in a novel bis [(perfluoroalkyl) sulfonyl] imide ionomer membrane." *Journal of the Electrochemical Society* 145.1 (1998): 107-110.
115. Tatsumisago, Masahiro, Kazuo Kishida, and Tsutomu Minami. "Preparation and proton-conduction of silica gels containing heteropoly acids." *Solid State Ionics*59.3-4 (1993): 171-174.
116. Shao, Zhi-Gang, et al. "Hybrid Nafion–inorganic oxides membrane doped with heteropolyacids for high temperature operation of proton exchange membrane fuel cell." *Solid State Ionics* 177.7 (2006): 779-785.
117. Checkiewicz, K., G. Zukowska, and W. Wieczorek. "Synthesis and characterization of the proton-conducting gels based on PVdF and PMMA matrixes doped with heteropolyacids." *Chemistry of*

materials 13.2 (2001): 379-384.

118. Magalad, Veeresh T., et al. "Preyssler type heteropolyacid-incorporated highly water-selective sodium alginate-based inorganic–organic hybrid membranes for pervaporation dehydration of ethanol." *Chemical Engineering Journal* 159.1 (2010): 75-83.
119. Yachandra, Vittal K., Kenneth Sauer, and Melvin P. Klein. "Manganese cluster in photosynthesis: where plants oxidize water to dioxygen." *Chemical Reviews*96.7 (1996): 2927-2950.
120. Stubbe, JoAnne. "Di-iron-tyrosyl radical ribonucleotide reductases." *Current opinion in chemical biology* 7.2 (2003): 183-188.
121. Riley, P. A. "Melanin." *The international journal of biochemistry & cell biology*29.11 (1997): 1235-1239.
122. Malik, Maqsood Ahmad, et al. "Oxidation of tyrosine by permanganate in presence of cetyltrimethylammonium bromide." *Colloids and Surfaces B: Biointerfaces* 76.1 (2010): 346-353.
123. Jang, Hyung-Seok, et al. "Tyrosine-mediated two-dimensional peptide assembly and its role as a bio-inspired catalytic scaffold." *Nature communications* 5 (2014).
124. Manceau, Alain, Matthew A. Marcus, and Sylvain Grangeon. "Determination of Mn valence states in mixed-valent manganates by XANES spectroscopy." *American Mineralogist* 97.5-6 (2012): 816-827.
125. Huang, Kun-Chang, et al. "Kinetics and mechanism of oxidation of tetrachloroethylene with permanganate." *Chemosphere* 46.6 (2002): 815-825.

126. Krapcho, A. Paul, James R. Larson, and Joyce M. Eldridge. "Potassium permanganate oxidations of terminal olefins and acetylenes to carboxylic acids of one less carbon." *The Journal of Organic Chemistry* 42.23 (1977): 3749-3753.
127. Huang, Xingkang, et al. "Preparation and properties of manganese oxide/carbon composites by reduction of potassium permanganate with acetylene black." *Journal of The Electrochemical Society* 154.1 (2007): A26-A33.
128. Goodwin, T. W., and R. A. Morton. "The spectrophotometric determination of tyrosine and tryptophan in proteins." *Biochemical Journal* 40.5-6 (1946): 628.
129. Suzuki, Hiroshi. *Electronic absorption spectra and geometry of organic molecules: An application of molecular orbital theory*. Elsevier, 2012.
130. Kalsi, P. S. *Spectroscopy of organic compounds*. New Age International, 2007.
131. Yamamoto, Takakazu. ". PI.-Conjugated Polymers Bearing Electronic and Optical Functionalities. Preparation by Organometallic Polycondensations, Properties, and Their Applications." *Bulletin of the Chemical Society of Japan*72.4 (1999): 621-638.
132. Omomo, Yoshitomo, et al. "Redoxable nanosheet crystallites of MnO2 derived via delamination of a layered manganese oxide." *Journal of the American Chemical Society* 125.12 (2003): 3568-3575.
133. Wang, Lianzhou, et al. "Inorganic multilayer films of manganese oxide nanosheets and aluminum polyoxocations: fabrication,

structure, and electrochemical behavior." *Chemistry of materials* 17.6 (2005): 1352-1357.

134. Barakat, Nasser AM, et al. "Preparation of nanofibers consisting of MnO/Mn3O4 by using the electrospinning technique: the nanofibers have two band-gap energies." *Applied Physics A* 95.3 (2009): 769-776.
135. Mayer, Lawrence M., Linda L. Schick, and Theodore C. Loder. "Dissolved protein fluorescence in two Maine estuaries." *Marine Chemistry* 64.3 (1999): 171-179.
136. Nevin, Austin, et al. "Analysis of protein-based binding media found in paintings using laser induced fluorescence spectroscopy." *Analytica chimica acta* 573 (2006): 341-346.
137. Kierdaszuk, Borys, et al. "FLUORESCENCE OF TYROSINE AND TRYPTOPHAN IN PROTEINS USING ONE-AND TWO-PHOTON EXCITATION." *Photochemistry and photobiology* 61.4 (1995): 319-324.
138. Heinecke, Jay W., et al. "Dityrosine, a specific marker of oxidation, is synthesized by the myeloperoxidase-hydrogen peroxide system of human neutrophils and macrophages." *Journal of Biological Chemistry* 268.6 (1993): 4069-4077.
139. Malencik, Dean A., and Sonia R. Anderson. "Fluorometric characterization of dityrosine: complex formation with boric acid and borate ion." *Biochemical and biophysical research communications* 178.1 (1991): 60-67.

국 문 초 록

단백질 기반의 생체모방 물질을 연구함에 있어서 중요한 주제 중 하나는 단백질을 구성하고 있는 아미노산에 따르는 단백질 구조의 접힘, 그리고 그로부터 결정되는 3차구조와 그 구조에 따라 달라지는 자기조립거동의 서열특이적 변화역학을 이해하는 일이다. 이러한 맥락에서 우리는 측쇄에 따라 달라지는 아미노산의 성질을 고려해 펩타이드를 디자인하고, 그 조립거동과 조립에 따른 자가조립체들의 특징들을 분석하였다. 파이-파이 쌓임을 일으키는 페닐알라닌, 2차원 구조 형성 경향성을 갖는 타이로신, 그리고 이합체 형성을 통해 대면적 조립거동의 단위체으로의 역할을 하는 시스테인을 모티프로 YFCFY라는 펩타이드를 디자인하였고, 이를 이용해 전에 없던 크고 평평한 2차원 시트를 공기와 물의 경계 표면에서 만들어 냈다. 사실, 펩타이드 자가조립을 통해 2차원 구조를 만들기 위해서는 통상적으로 시트형태의 뭉침 현상을 잘 일으키는 베타시트 형성 서열을 이용하는 것이 일반적이다. 그러나 본 연구에서는 나선형 구조로도 단위체들이 잘 정렬된 시트형태의 2차원 대면적 구조체를 만들 수 있다는 것을 보여주었다. 게다가 이 YFCFY 펩타이드는 물방울 표면에서 높은 탄성계수를 갖는 10nm의 균일한 나노시트를 만드는데, 이 잘 조립된 2차원 시트는 다양한 기판에 옮겨질 수 있으며 그 위에 다른 기능적인 요소를 부여할 수 있는 장점을 가진다. 이러한 특성은 YFCFY nano sheet가 원하는 기능을 부여하는 다른 공정과정과 결합할 수 있다면, 바이오센서, 촉매 등과 같은 생화학적 기능을 갖는 바이오 플랫폼으로 사용될 수 있는 가능성을 보여준다. 여기에서 그치지

않고, 본 연구에서는 이와 같은 2차원 펩타이드 물질의 활용가능성을 좀 더 구체적으로 제시하기 위해 자연계에서의 타이로신이 중요한 역할을 하고 있는 화학 반응들과 멜라닌과 같은 최송산물을 만드는 중합 반응 등에 기반해 펩타이드 물질에 기능을 부여하고자 하는 시도를 하였다. YFCFY와 유사한 성질의 YYACAYY 펩타이드 기반 2차원 재료와 Mn^{+7}을 포함한 산화제와의 산화반응을 통해 망간 산화물과의 하이브리드를 새롭게 합성하였다. 여러 가지의 분석 도구들을 통해 새로이 합성된 물질의 재료 및 전기적 특성을 면밀히 분석한 결과 이 물질이 높은 수준의 양성자 전도도성을 갖는 물질임을 밝혔고, 더불어 양성자 전도체 디바이스로의 활용 가능성 또한 제시하였다. 위와 같은 일련의 연구를 통하여, 본 연구에서는 통상적인 타이로신의 역할로 알려져 있는 어셈블리 모티프와 자연계에서 프로톤 채널을 만드는 매개체로의 타이로신의 역할이 결합될 수 있다는 것을 보여주고자 하였다.

A short story in a very personal voice

문장이나 구(phrase) 등의 끝을 다루는 방법을 일컬어 구두법이라고 하는데, 영어 단어로는 punctuation이라고 한다. comma(,)나 semi-colon(;)처럼 단어 대신 직접 바꾸어 쓸 수 있는 구체적 형태가 있는 것들에 비해, punctuation은 이들을 묶어 '대표성'이라는 추상적인 껍데기를 한 겹 더 걸쳤다. 때문에 이 단어 자체만을 기억 속에서 꺼내볼 일이 딱히 없어, 단어를 마주하자니 살짝 낯선 느낌이 든다.

구두점 중에 가장 많이 쓰이는 건 뭘까? 띄어 쓰기를 제외하면, 마침표와 쉼표 둘 중 하나일 것 같다. 마침표는 영어로 period인데, 사실 period는 기간이나 주기라는 뜻으로 더 많이 쓰인다. 내 메일 주소 끝에 오는 닷컴의 'dot'이란 단어가 오히려 마침표와 어울리는 것 같다. period의 어원은 periodos라는 궤도, 코스라는 뜻의 라틴어인데, around라는 뜻의 접두사 peri와 way라는 뜻의 hodos가 함께 녹아 생긴 말이다. 병의 재발이라는 뜻으로도 쓰였다고 한다. 슬금슬금 바뀌어온 이런 모양새를 더듬다 보니, 기간이나 주기라는 뜻들이 '마침'과 전혀 관계가 없는 것 같지만은 않다. 시간들을 모아 그 끝에 마침표 하나를 놓아야지만 비로소 '무엇을 했던 기간'이라고 표현할 수 있게 됨을 떠올려보면.

모양새가 마치 언어학으로 학위를 받는가 싶게 되어가는 것 같지만, 다시 구두법으로 돌아와본다. 굉장히 사소해 보여도 역사의 발전에 의외로 큰 파이를 차지하고 있는 것이 이 구두법이다. 스스로 어떤 계몽의 빛을 내는 항성 같은 존재는 아니지만, 수많은 쓰여짐 속에서 구두점들은 독자에게 '명료함'을 제공해왔다. 앞과 뒤를 구분해 물리적으로 생각할 공간을 제공하고, 때로는 그 다음의 줄 세워진 글자들을 어떻게 바라보아야 하는 지에 대한 방향도 제시해준다. 기록물에 대한 이해 효율을 높이는 데 적잖이 보탬을 한 것으로 인정받는다.

마르셀 프루스트의 '잃어버린 시간을 찾아서'라는 작품이 있다. 프랑스 문학의 정수이자 20세기 최고의 작품이라는 찬사를 받는 작품이다. 시대를 풍미하는 작가의 우아한 철학이 담긴 이 책은, 세 페이지 당 하나의 마침표가 등장하는, 작품 전반에 걸친 미칠 듯한 긴 호흡을 통해 독자에게 절망을 불어넣는 것으로 사실 더 유명하다. 우리는 프루스트의 한 문장을 읽기 위해 숨막히는 세 페이지의 여정을 감내해야 하는 것이다. 인생 읽기에 있어서도 마찬가지가 아닐까 한다. 인생의 단락에 적절한 구두점들이 없다면, 특히 마침표의 등장이 제때 이루어지지 않는다면, 우리는 가쁜 숨을 몰아 쉬며 난해함에 파묻힌 삶의 의미들을 읽어내야만 할 것이다. (비록 그 전체가 훌륭한 대작일지라도) 구두

점들은 시간과 기억, 감정들을 선택적으로 수집해 압축하고, 다른 시간들과는 분리해 마음을 쓰도록 한다. 띄어 쓴 칸에서 숨을 고르고, 쉼표에서 맥락을 점검하며, 마침표에서 우리는 고개를 들고 달려온 길과 나아갈 길의 방향에 대한 고민을 시작하는 것이다. 그렇게 우리는 보다 효율적으로 인생을 읽고, 해석하며 이해하게 된다.

우리는 예기치 못하게 태어났고, 시간이 우리의 뜻과는 상관없이 그리고 끊임없이 흐르는 세상 속에서 삶을 짓고 있다. 쉬지 않고 밀려드는 미래가 오늘이 되는 삶의 해안가에서 언제, 어디에, 어떤 구두점을 찍어야 하는가에 대한 구체적 고민을 할 여유를 갖는 것은 참 쉽지가 않다. 제도적으로 혹은 물리적으로 변화를 겪는 시점에 점 비슷한 것 찍는 것도 어려워하며 정신 없이 사는 것이 고작일지도 모른다. 마침표를 찍었는데 돌아보니 쉼표였어야 했던 곳도 있을 것이고, 적당히 채워 놓은 시기에 마침표를 찍을 자리를 찾지 못해 결국 문장이 될 수 없던 시간들도 있을 것이다.

검색 엔진에 '학사 석사 박사 교수'라고 입력하면 찾을 수 있는 유머가 있다. 학사: 들은 적은 있으나 설명할 수 없는 상태, 석사: 이제 무엇을 모르는지 아는 상태, 박사: 나만 모르는 줄 알았는데 남들도 다 모른다는 걸 아는 상태. 이에 따르면, 나는 많은 날을 지불하여 석사생활에 마침표를 찍고, 영수증으로는 내가 모른다는 그 사실만 알게 된 셈이다. 다른 이들은 어떨지 모르겠지만, 무지 속에서 헤매던 나의 지난 시간들을 떠올려보면 저 말을 부인하기가 어렵다. 2년 반을 묵직하게 뭉친, 그러나 내세울 것은 딱히 없는 단락에 마침표를 찍는 이 순간에 서서 고개를 들어본다. 지금 시야에는 물음표가 가득 달린 나무들만이 자리하고 있지만, 나는 인생이란 숲이 어떤 것일까 상상해 본다. 언젠가는 잘 묶여진 이 시간들이 내게 남기는 어떤 의미가, 숲을 이해하는 데 있어서 문 하나쯤 열어줄 수 있는 열쇠가 되지는 않을까 생각해본다.

혼자서는 결코 도착하지 못했을 이 곳에, 받았던 모든 따뜻한 마음들을 담아 온기 어린 마침표를 찍는다.

2017년 2월
최익랑 씀